NASA NAGW-1968

Study of Atmospheric and Bidirectional Effects on Surface Reflectance and Vegetation Index Time Series: Application to NOAA AVHRR and Preparation for Future Space Missions

-Final Report-

Principal Investigator
Robert Frouin
California Space Institute
Scripps Institution of Oceanography
La Jolla, California 92093-0221

June 14, 1993

The objectives of our investigation, namely *"to characterize the atmospheric and directional effects on surface reflectance and vegetation index using the First ISLCSP Field Experiment (FIFE) dataset, develop new algorithms to obtain better AVHRR indices, and define possible improvements for future satellite missions"*, have been addressed in three separate, yet complementary studies.

First, we have shown, from theoretical calculations, that visible and near-infrared reflectances combined linearly at optimum (one or two) viewing angles relate linearly to the fraction of photosynthetically available radiation absorbed by plants, f_{par}, can be used independently of the type of foliage and substrate, eliminate the effects of sub-pixel spatial heterogeneity, and improve the accuracy of the f_{par} estimates when compared to the Normalized Difference Vegetation Index, NDVI.

Second, we have demonstrated that NDVI, even though it is not a linear combination of radiances or reflectances, can be spatially integrated without significant loss of information from scales of 300 to 1000m.

Third, we have successfully modeled AVHRR visible and near-infrared reflectances over the FIFE site, separating temporal and bidirectional components and determining the model parameters through an original iterative scheme. It appears that NDVI generated from the top-of-atmosphere reflectances normalized by the bidirectional effects (as determined in the scheme) is a better vegetation index than maximum NDVI.

Details about the three studies are given below.

1. Photosynthetically Available Radiation Absorbed by Plants

We have completed a study of optimum combinations of visible and near-infrared reflectances for estimating the fraction of photosynthetically available radiation absorbed by plants, f_{par}. The results, published in the Proceedings of the 5th International Colloquium on Physical Measurements and Signatures in Remote Sensing (Podaire et al., 1991; see appendix 1), strongly suggest that linear combinations of visible and near-infrared reflectances at specific viewing angles may be more accurate in predicting f_{par} than vegetation indices that are non-linear functions of radiance or reflectance such as NDVI and the simple ratio, SR. For a sun at 60° from zenith in July at 45°N, for instance, the f_{par} residual error is reduced from 0.058 to 0.033 (a factor of about 2). When using NDVI the minimum residual error is obtained for a nadir viewing, but when using linear combinations it is preferable to view the canopy at a 45° zenith angle.

2. Spatial Integration of NDVI

We have investigated the effect of spatial heterogeneity on the spatial integration of NDVI, which has concretized in an article published in IEEE Geoscience and Remote Sensing (Aman et al., 1991; see Appendix 2). For the considered sites, located in tropical West Africa and temperate France, and the scales analysed, 300 to 1000m, we have found that a strong correlation exists between NDVI calculated from average reflectances, M_{NDVI}, and NDVI integrated from

individual NDVIs, I_{NDVI}. The relationship is almost perfectly linear, with a slope depending slightly on the variability of the vegetation cover. Effecting the scale change using M_{NDVI} instead of I_{NDVI} does not introduce significant errors, especially when these errors are compared to those resulting from uncertainties in the relationships between NDVI and vegetation parameters, which are typically one order of magnitude higher. It is not excluded, however, that the principal scales of variability are smaller than the size of the pixels used in the calculations (20 to 30m), and other sites should be examined, as well as the variability of the vegetation below 30 m, to conclude definitely and generally about the adequacy of using M_{NDVI} in biophysical parameterizations obtained at the local scale.

3. Surface reflectance and NDVI modeling

Regarding our analysis of AVHRR data during FIFE, we have successfully modeled the channel 1 (visible) and channel 2 (near-infrared) reflectances. First, the data were carefully cloud-screened (Figs 1a, 1b, 1c, 1d). This was done by examining the relationship between spatial standard deviation and average value over the FIFE site in channels 1 and 4 (thermal infrared) (Figs. 1a and 1b), average values in channels 1 and 4 (Fig. 1c), and spatial standard deviations in channels 1 and 4 (Fig. 1d). Identifying on the plots the clear and cloudy cases as observed by an all-sky camera, we found that thresholds of 4 $Wm^{-2}sr^{-1}\mu m$ and 0.2 $mWcm^{-2}sr^{-1}cm$ for the standard deviations in channels 1 and 4, respectively, provided the best cloud screening. All the data corresponding to channel 1 or channel 4 standard deviations above the threshold values were eliminated. Figs. 2, 3, and 4 illustrate the quality of the cloud-screening. Second, the raw data was transformed into reflectance (Fig. 5), from which was generated NDVI (Fig. 6). In the transformation, we took into account the drift in time of the AVHRR sensor according to Whitlock et al. (1990). It is interesting to note that the large variations in reflectance over a few days (Fig. 5), which camouflage any long-term trend, especially in the near-infrared (Fig. 5b), are substantially reduced when the visible and near-infrared reflectances are combined into NDVI (Fig. 6). The seasonal cycle of the vegetation becomes apparent, with high NDVI values in summer and low values in winter. Third, we expressed top-of-atmosphere reflectance as the product of a constant ,R_0, and normalized temporal and bidirectional functions, F and G, respectively. Fig. 7 gives the model equations. For G, we used the simplest parameterization possible: G is expressed as the sum of a Lambertian contribution, a term corresponding to isotropic scattering in a semi-transparent medium (vegetation canopy), and a term taking into account the effect of shadowing structures. For F, we used a Fourier series limited to the 5th order (higher harmonics did not improve the accuracy of the modeling). Fig. 8 gives a shematic description of the iterative scheme developed to determine the model parameters. The bidirectional and temporal components of the model are estimated successively by linear, multivariate regression, and after a number of iterations, typically 10, convergence is obtained (see Fig. 9). Applying the model to the FIFE data, we explain 95% of the variance in both the visible and near-infrared channels (Fig. 10). Table 1 displays the model parameters, and Table 2 summarizes the comparison statistics between modeled and observed reflectances. The correlation coefficient is close to 0.98 for both channels and the standard deviation before

regression is reduced from 0.45 to 0.10 and 0.21 to 0.01 in the visible and near-infrared channels, respectively. Fig. 11 shows $R_0F(t)$ as a function of time, and Fig. 12 the resulting NDVI, $NDVI_t$. Although $R_0F(t)$ and $NDVI_t$ are still contaminated by atmospheric effects (water vapor absorption and aerosol and molecular scattering), there are independent of solar and viewing geometries, which makes them useful to monitor the time changes of the earth's surface. In Fig. 11, for instance, a minimum of reflectance in the visible and a maximum in the near-infrared are observed during summer , and these features were not apparent in the raw data (Fig. 5). In Fig. 12, the effect of vegetation stress around Julian day 220 (resulting from a lack of rain) is well depicted, but this stress could not be detected in the raw NDVI time series (Fig. 6). A strong correlation exists between observed NDVI and modeled $NDVI_t$ (Fig. 13), but the standard deviation remains rather large (12.5%) of the average NDVI value. Figs. 14 and 15 compare maximum NDVIs over 11 day periods (without and after cloud-filtering) and $NDVI_t$, respectively. The correlation coefficients are large (above 0.98), but significant biases exist, especially when unfiltered data are used. It appears, for the dataset analysed, that the simple procedure of averaging cloud-filtered NDVI data yields better results than maximum NDVI (Fig. 16 and Table 3).

Appendix 2

Upscale Integration of Normalized Difference Vegetation Index: The Problem of Spatial Heterogeneity

A. Aman, H. P. Randriamanantena, A. Podaire, and R. Frouin

(!EEE Transactions on Geoscience and Remote Sensing, Vol. 30, No. 2, 326-338, March 1992)

Table 1. Top-of-atmosphere reflectance model parameters.

Model Parameters	Channel	
	Visible	Near-Infrared
Constant		
R_0	.1153	.2178
Bidirectional		
g_1	.1241	.1209
g_2	.4800	.3725
Temporal		
A_1	.1216	−.2994
A_2	−.0589	.0451
A_3	−.0004	.0071
A_4	.0515	.0043
A_5	.0851	.0388
B_1	.1668	.0127
B_2	.0706	.0315
B_3	−.0351	.0820
B_4	.0175	−.0337
B_5	.0170	−.0090

Table 2. Comparison statistics between measured and modeled NOAA-9 AVHRR reflectance.

Parameter	Channel	
	Visible	Near-Infrared
Number of Points	91	91
Correlation Coefficient	.979	.977
Standard Deviation (before Regression)	.0452	.2119
Standard Error	.0102	.0142
Explained Variance (%)	94.9	95.5

Table 3. Comparison statistics between maximum NDVI (without cloud-filtering) and modeled NDVIt (case 1), between maximum NDVI (after cloud-filtering) and modeled $NDVI_t$ (case 2), and between average NDVI (after cloud-filtering) and modeled $NDVI_t$ (case 3).

Parameter	Case 1	Case 2	Case 3
Number of Points	29	28	28
Correlation Coefficient	.985	.977	.980
Standard Deviation (before Regression)	.152	.148	.137
Standard Error	.051	.045	.028
Residual Error	.026	.031	.028
Bias (Measured - Modeled)	.043	.032	.006
Explained Variance	97.0	95.5	96.1

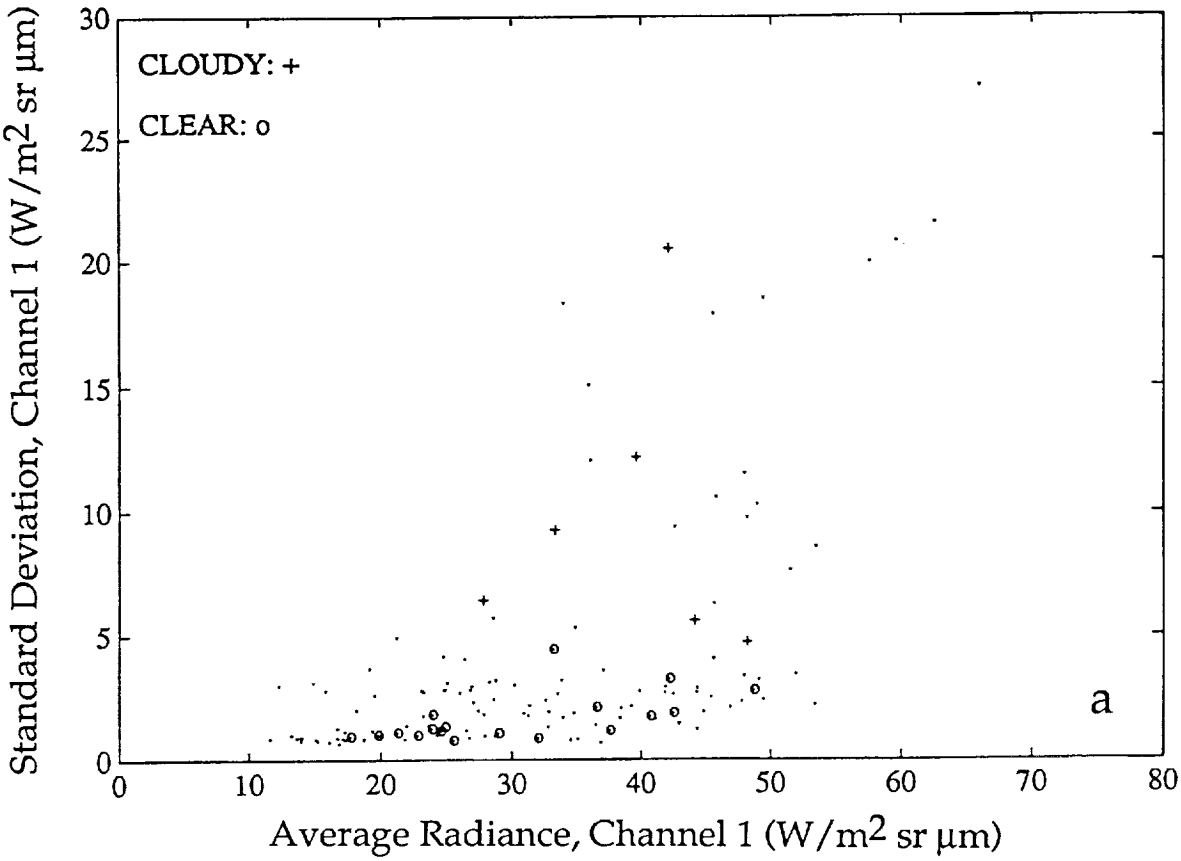

Fig. 1a. Standard deviation of NOAA-9 AVHRR channel 1 (visible) radiance over the FIFE site versus average radiance.

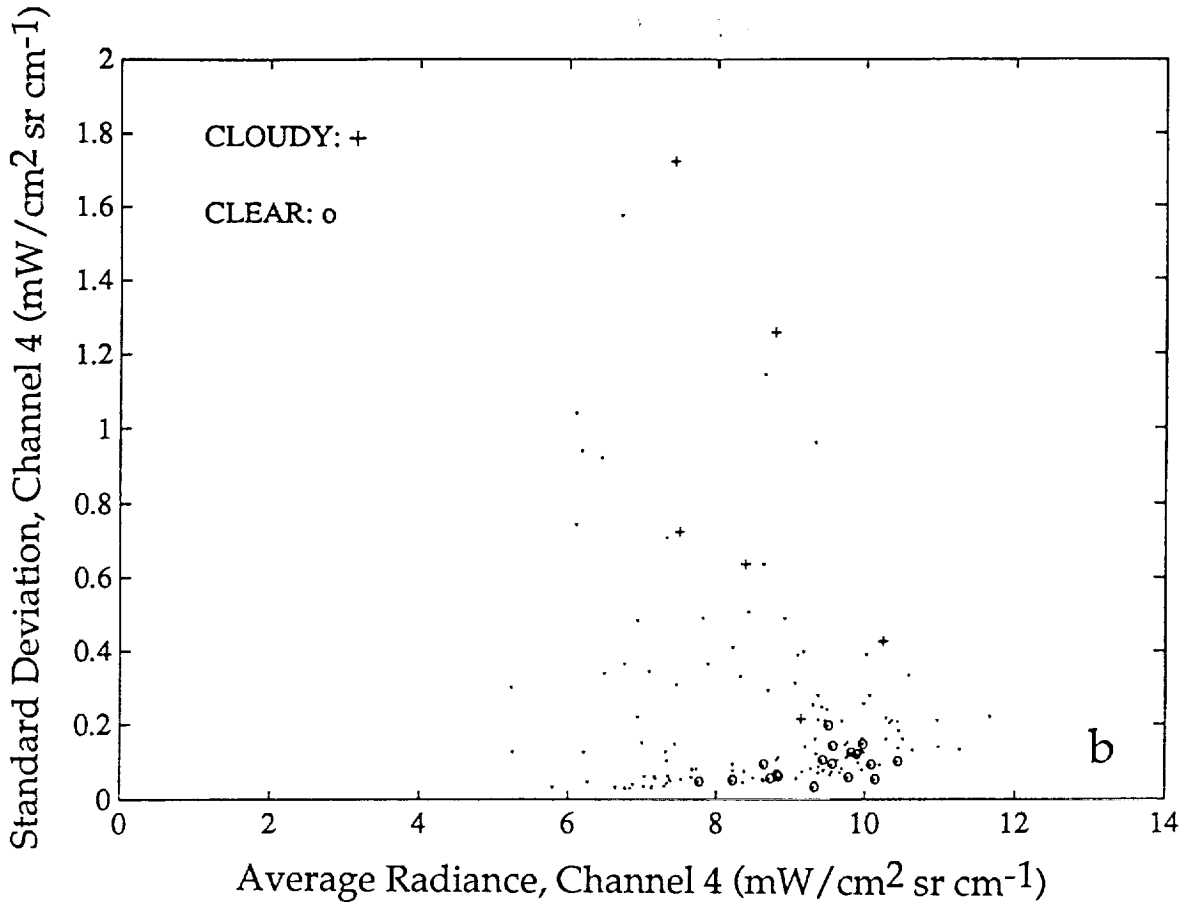

Fig. 1b. Standard deviation of NOAA-9 AVHRR channel 4 (thermal infrared) over the FIFE site versus average radiance.

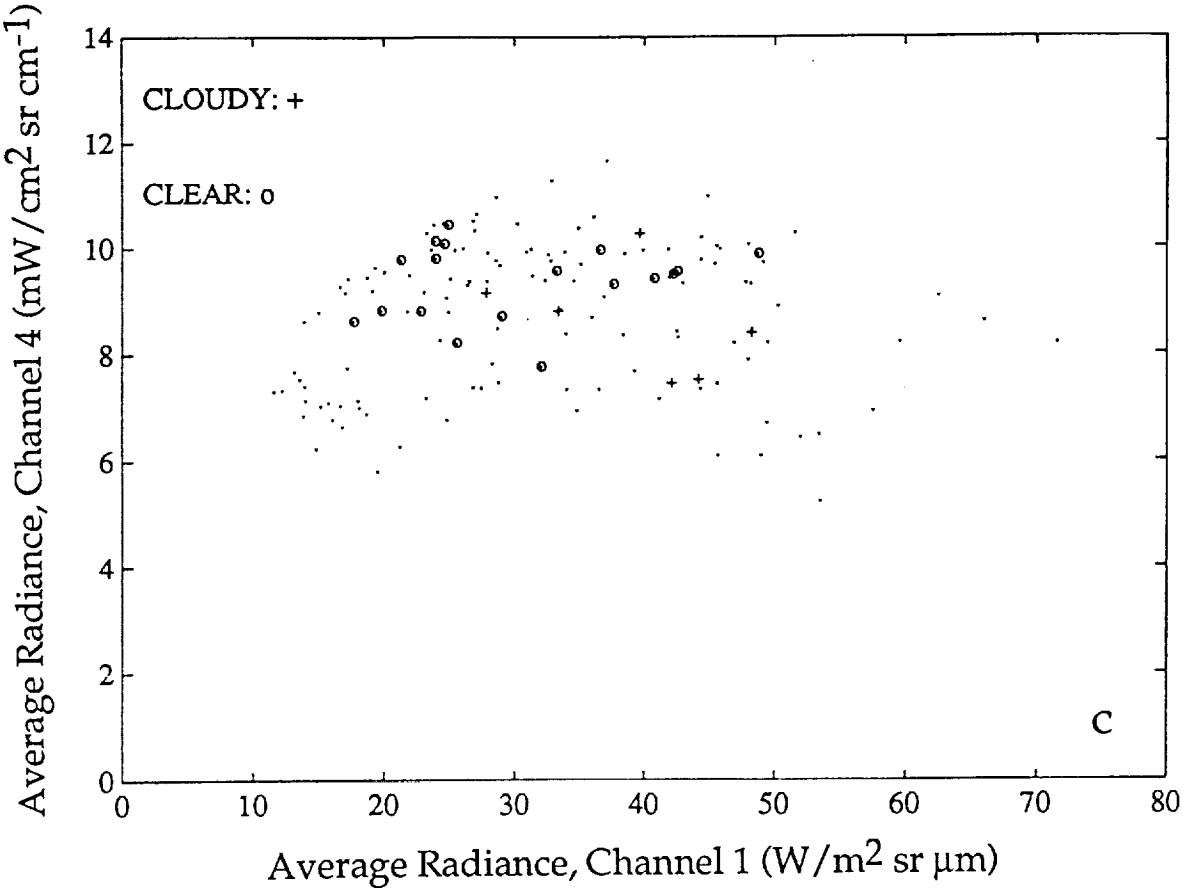

Fig. 1c. Average NOAA-9 AVHRR channel 4 (thermal infrared) radiance over the FIFE site versus average channel 1 (visible) radiance.

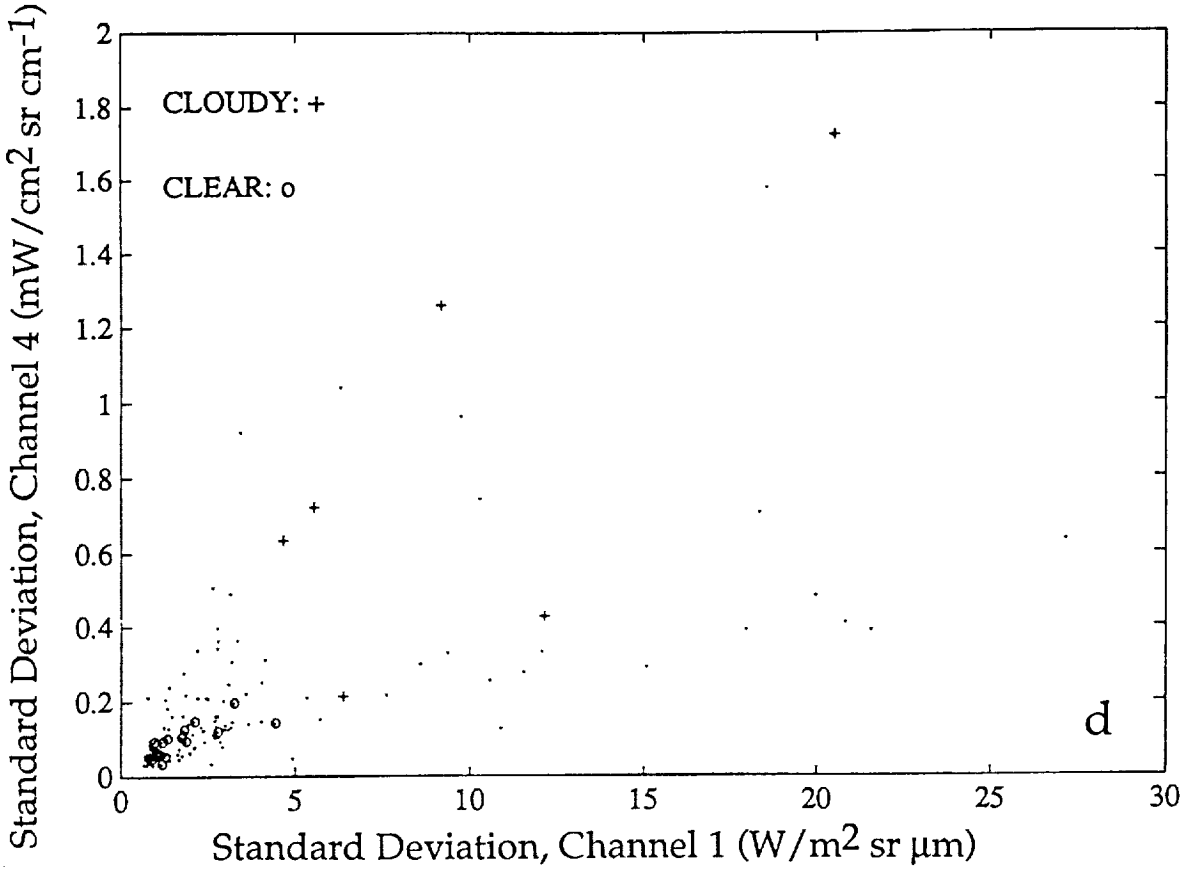

Fig. 1d. Standard deviation of NOAA-9 AVHRR channel 4 (thermal infrared) radiance over the FIFE site versus standard deviation of channel 1 (visible) radiance.

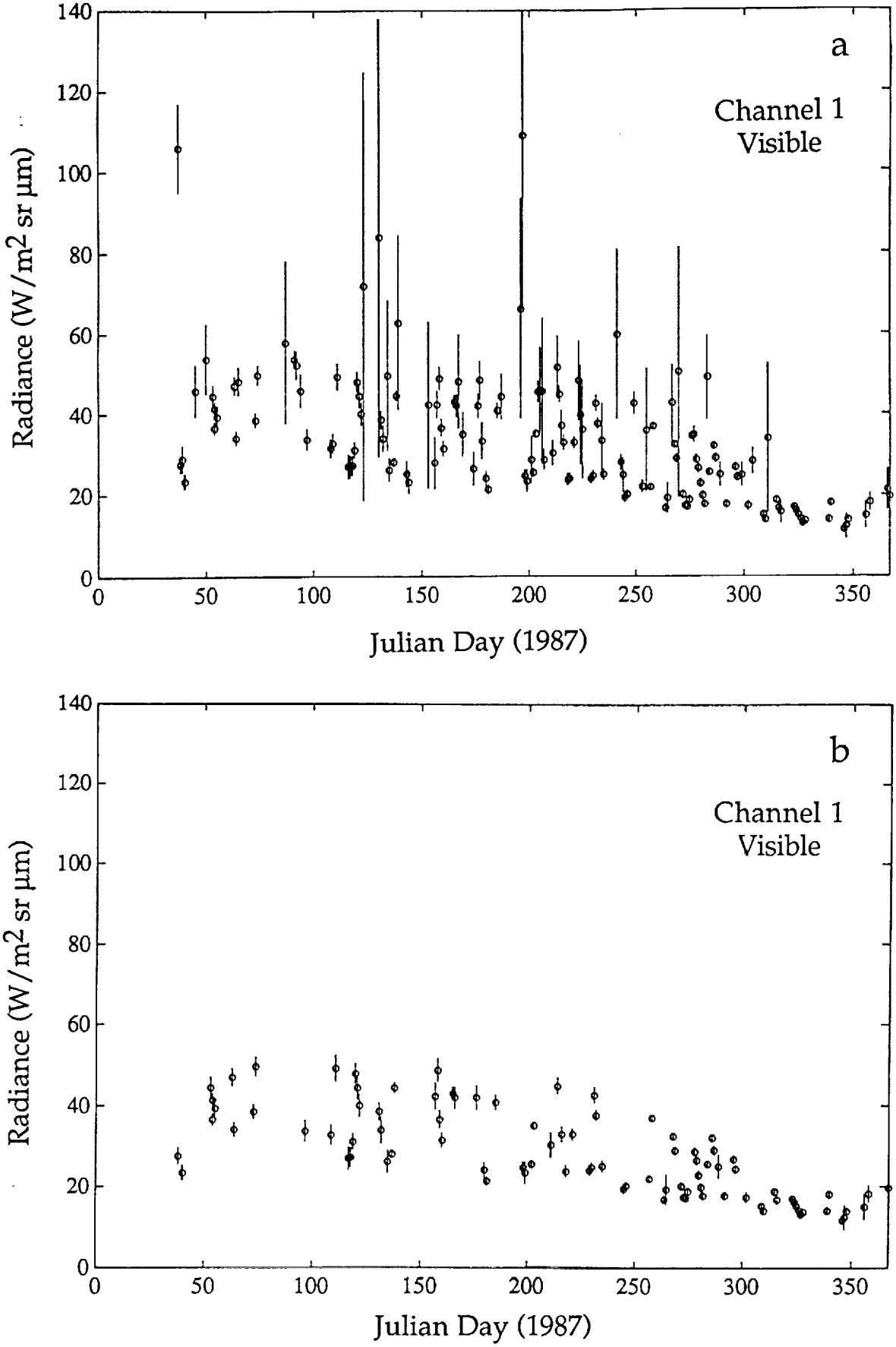

Fig. 2. Time series of average NOAA-9 AVHRR channel 1 (visible) radiance over the FIFE site during 1987. (a) raw data; (b) cloud-filtered data.

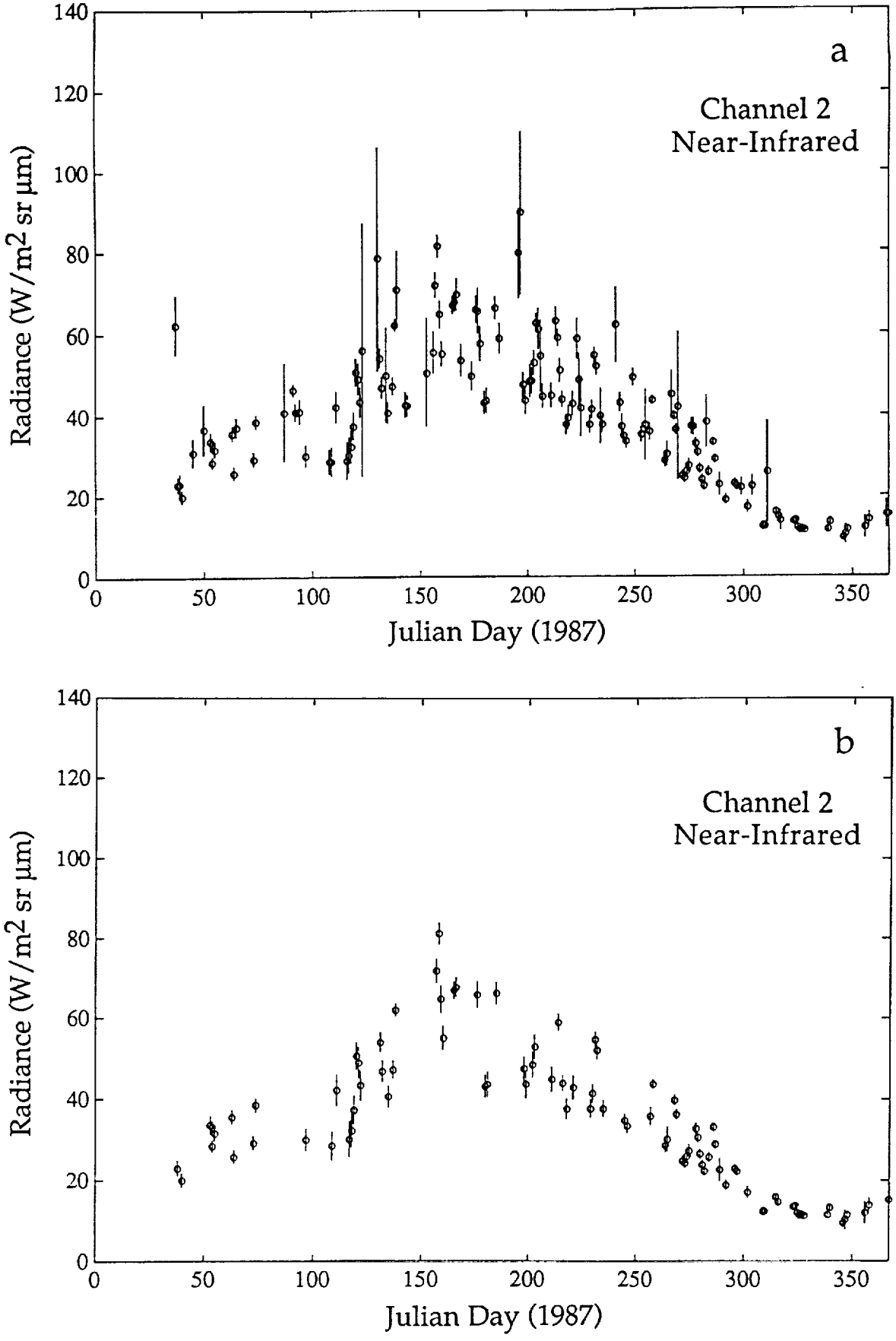

Fig. 3. Time series of average NOAA-9 AVHRR channel 2 (near-infrared) radiance over the FIFE site during 1987. (a) raw data; (b) cloud-filtered data.

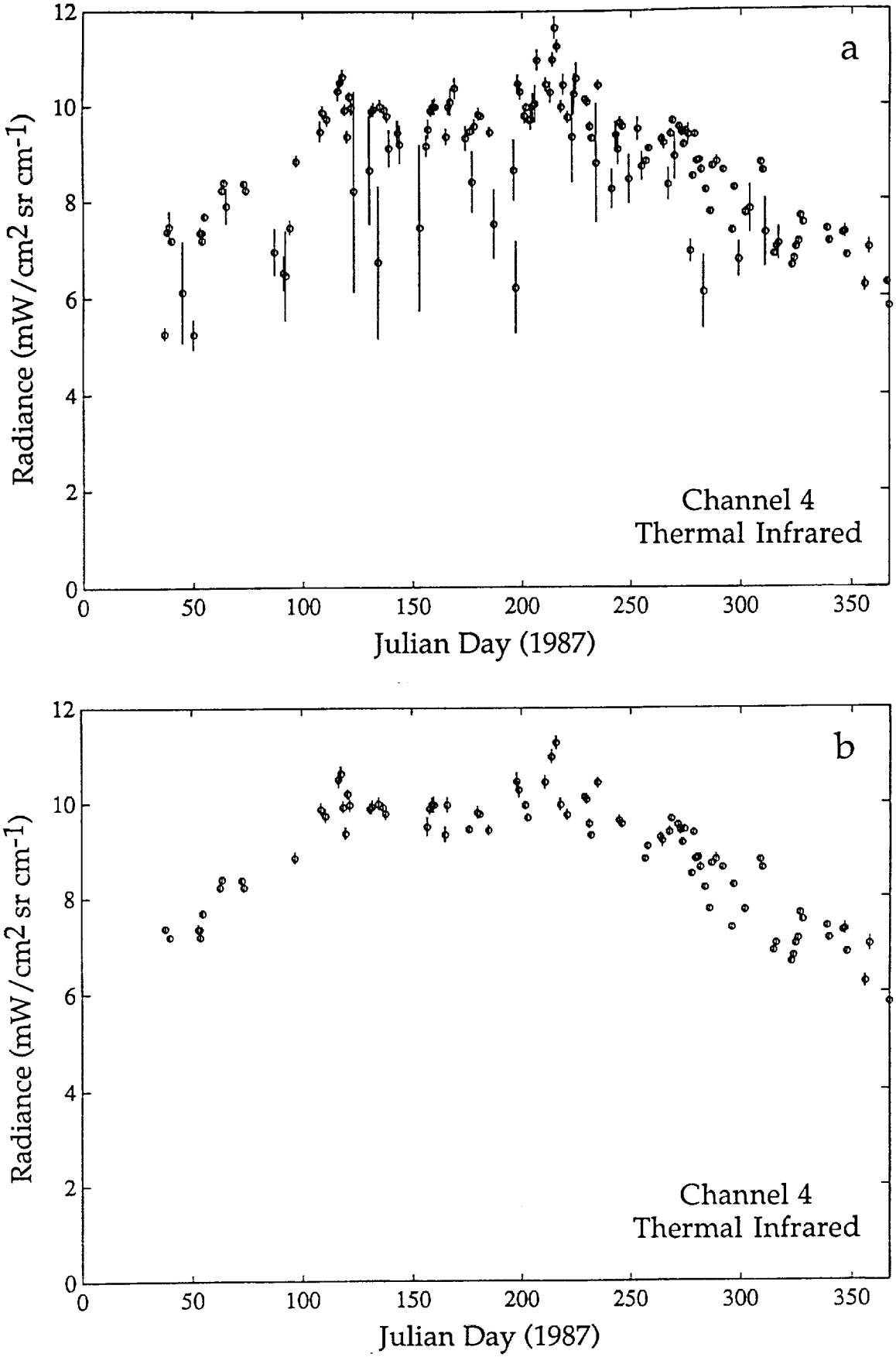

Fig. 4. Time series of average NOAA-9 AVHRR channel 4 (thermal infrared) radiance over the FIFE site during 1987. (a) raw data; (b) cloud-filtered data.

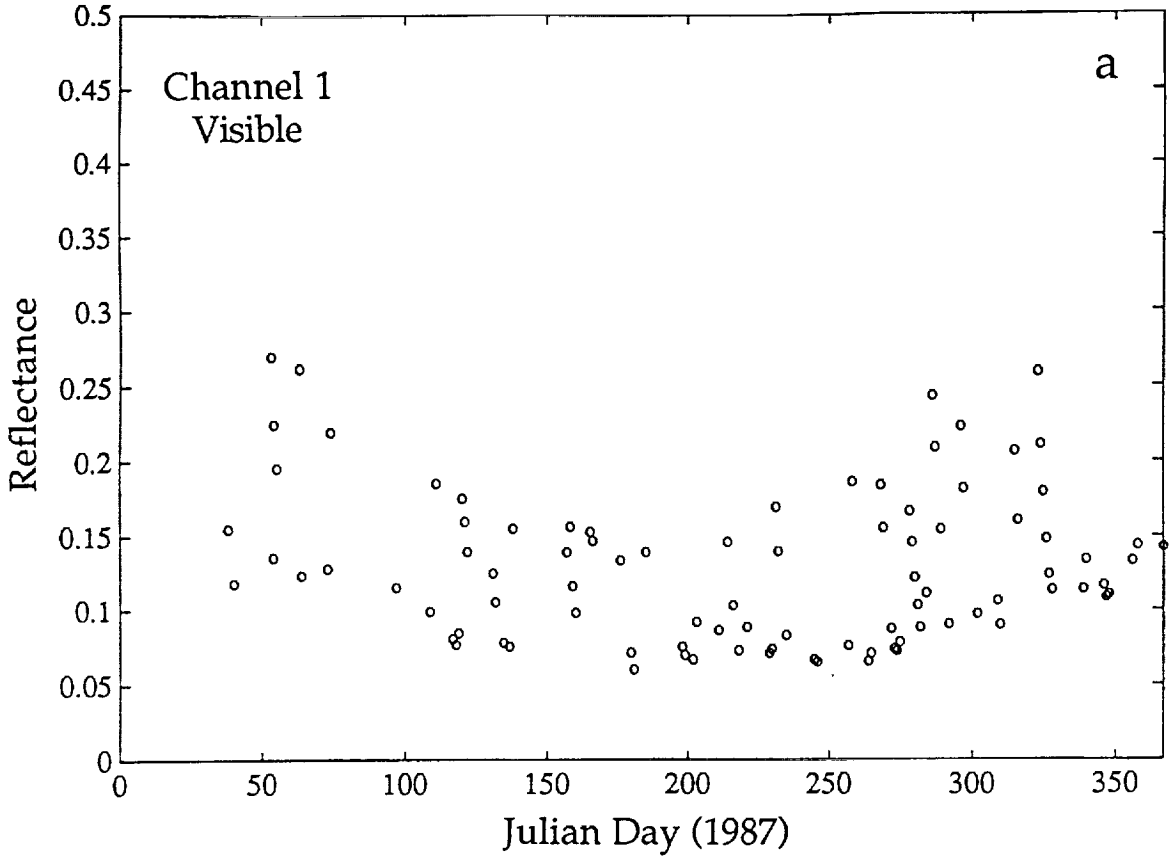

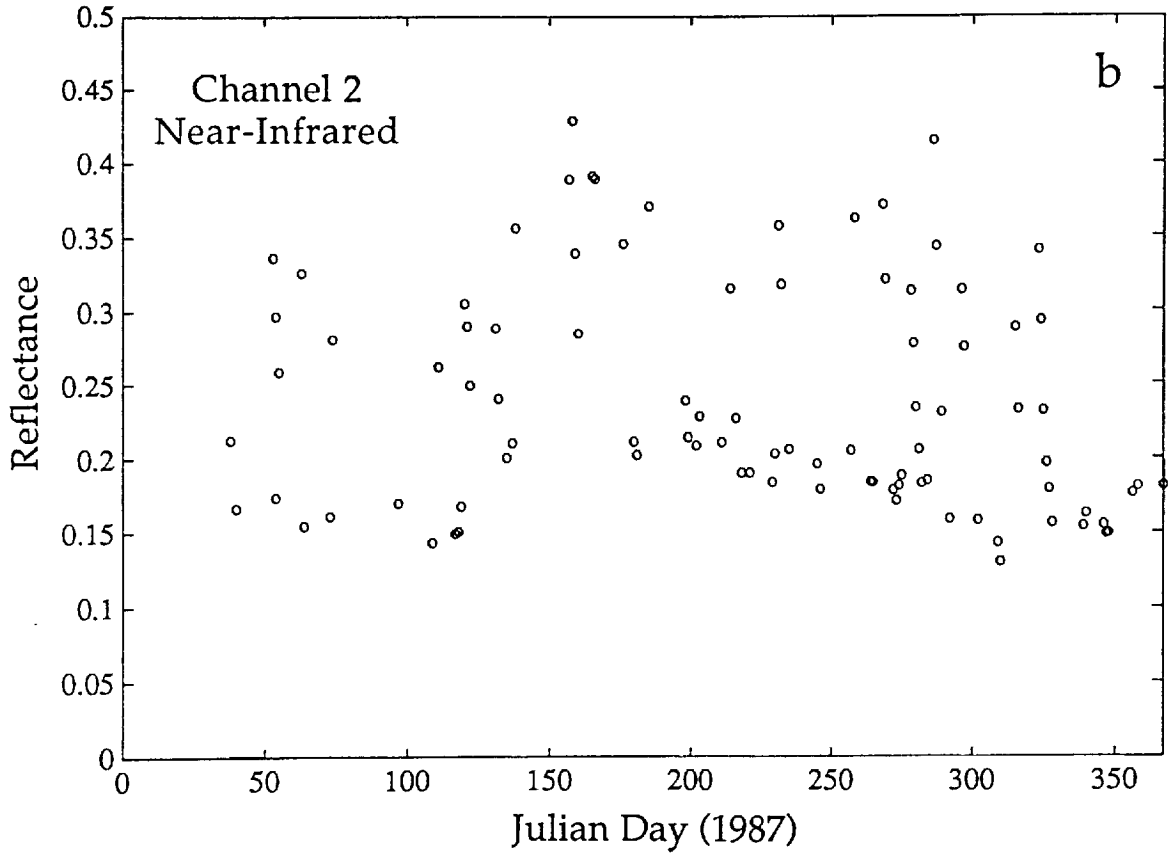

Fig. 5. Time series of cloud-filtered average NOAA-9 AVHRR reflectances over the FIFE site during 1987. (a) channel 1 (visible); (b) channel 2 (near-infrared).

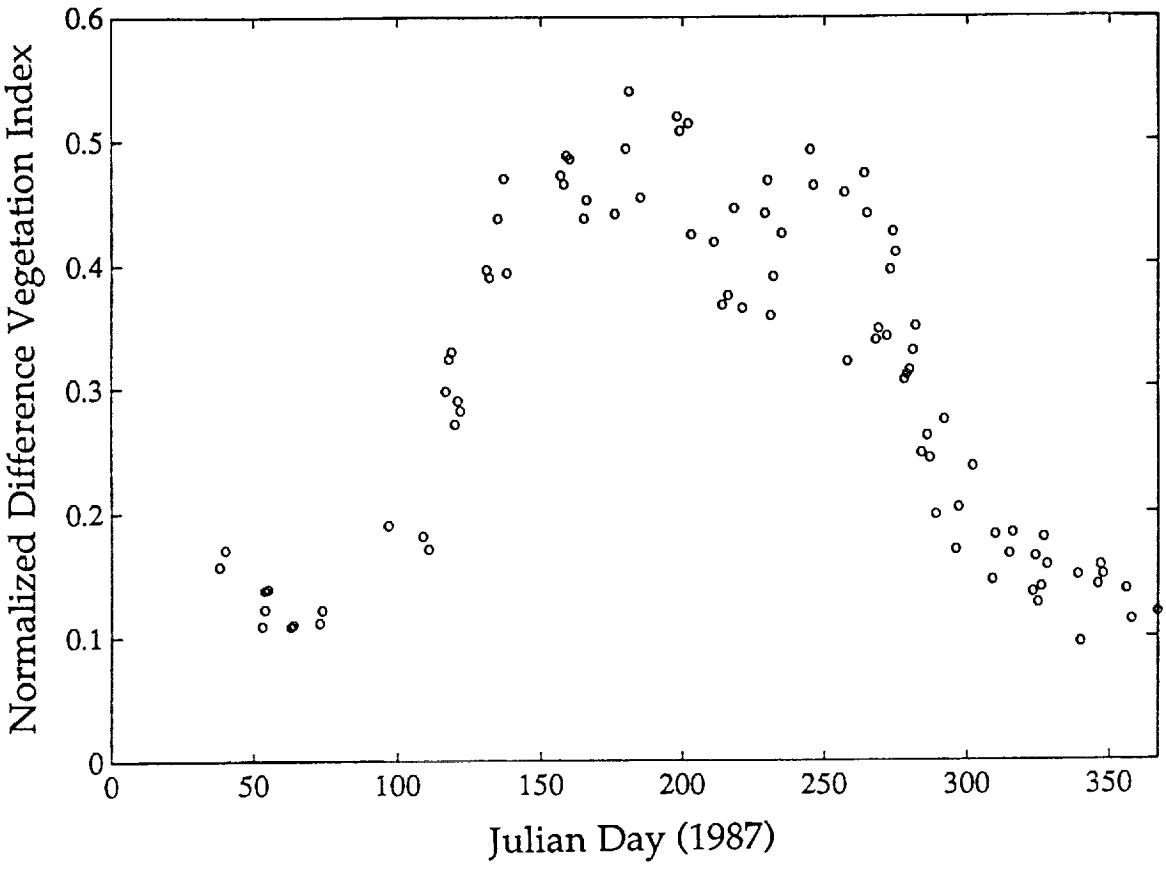

Fig. 6. Cloud-filtered time series of NOAA-9 AVHRR-derived normalized difference vegetation index over the FIFE site during 1987.

$$R(t;\theta_s,\theta_v,\phi_s-\phi_v) = R_o\, F(t)\, G(\theta_s,\theta_v,\phi_s-\phi_v)$$

$$F(t) = 1 + \sum_{i=1}^{N}\left[A_i \cos\left(2\pi i \frac{t}{T}\right) - \frac{1}{P}\sum_{j=1}^{P}\cos\left(2\pi i \frac{t_j}{T}\right)\right] + \sum_{i=1}^{N}\left[B_i \sin\left(2\pi i \frac{t}{T}\right) - \frac{1}{P}\sum_{j=1}^{P}\sin\left(2\pi i \frac{t_j}{T}\right)\right]$$

$$G(\theta_s,\theta_v,\phi_s-\phi_v) = 1 + g_1 f_1(\theta_s,\theta_v) + g_2 f_2(\theta_s,\theta_v,\phi_s-\phi_v)$$

$$f_1(\theta_s,\theta_v) = \frac{1}{\cos\theta_s \cos\theta_v} - \frac{1}{\frac{1}{P}\sum_{j=1}^{P}\cos\theta_{sj}\cos\theta_{vj}}$$

$$f_2(\theta_s,\theta_v,\phi_s-\phi_v) = \sin\theta_s \sin\theta_v \cos(\phi_s-\phi_v) - \frac{1}{P}\sum_{j=1}^{P}\sin\theta_{sj}\sin\theta_{vj}\cos(\phi_{sj}-\phi_{vj})$$

Fig. 7. Top-of-atmosphere reflectance model. Reflectance is expressed as the product of a constant, R_o, and normalized temporal and bidirectional functions, F and G. In the equations, t is time, T is the length of the dataset, P is the number of observations, N is the number of harmonics for F, and indices i and j refer to harmonics and observations, respectively.

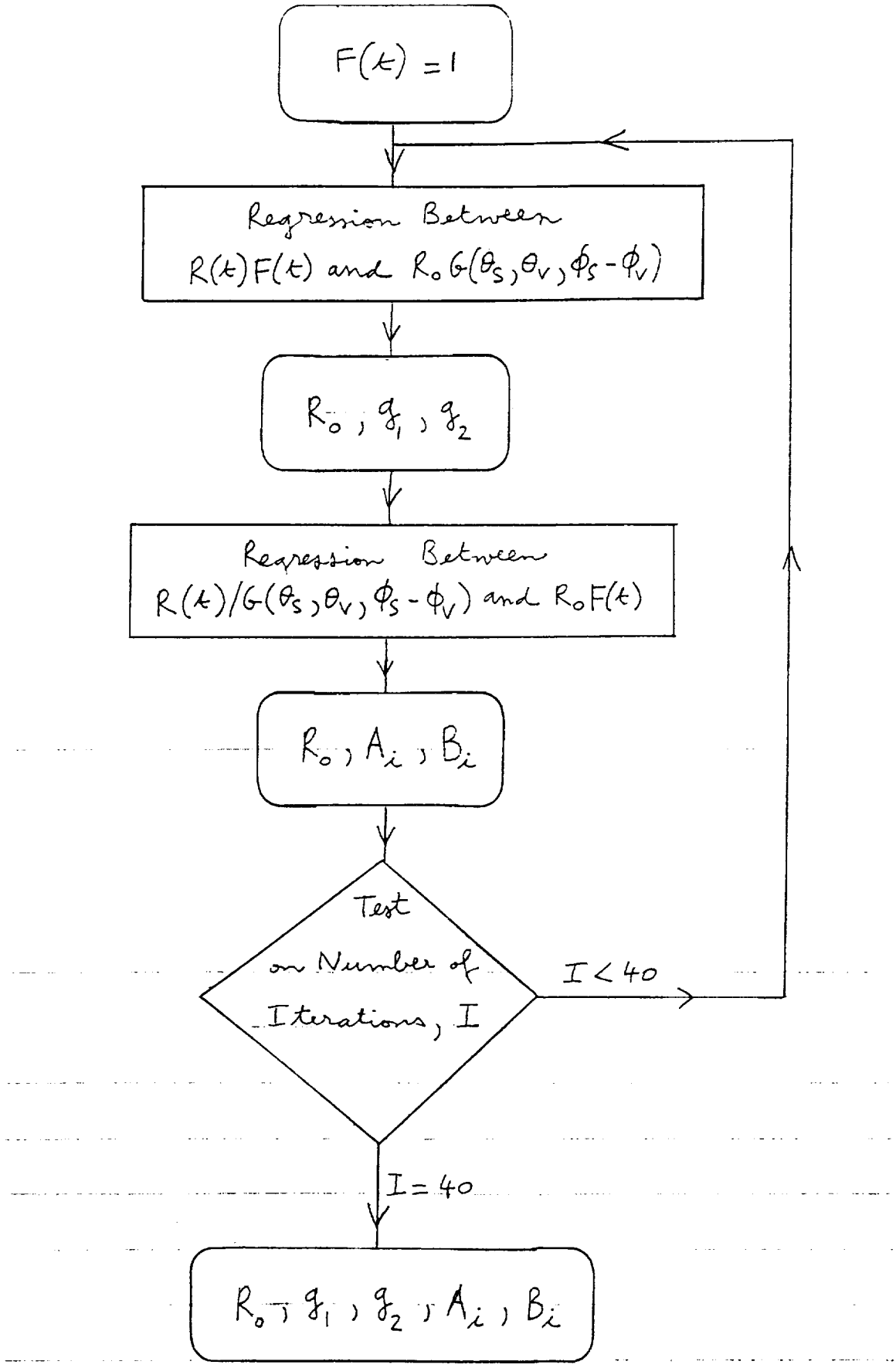

Fig. 8. Iterative algorithm to determine the reflectance model parameters.

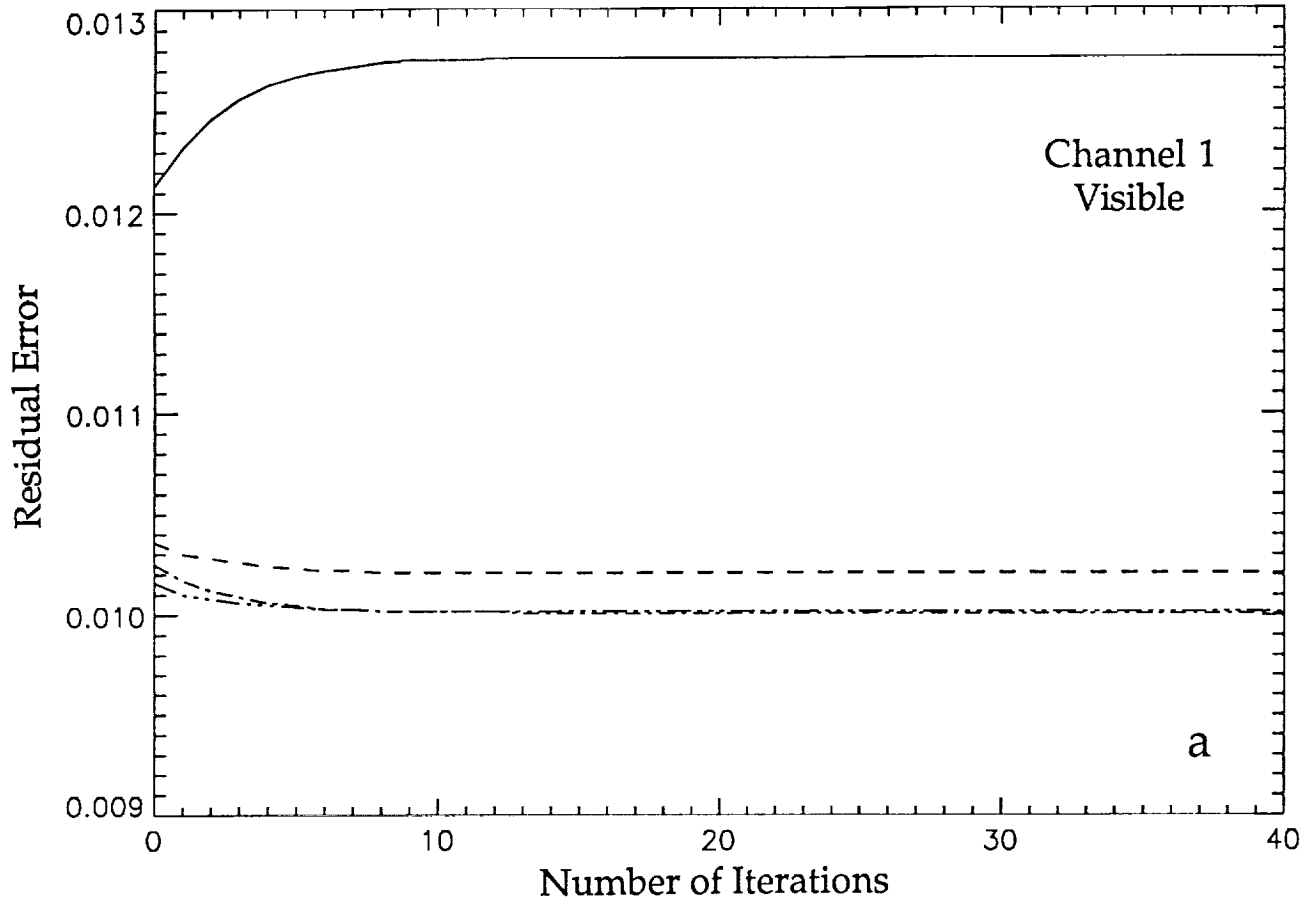

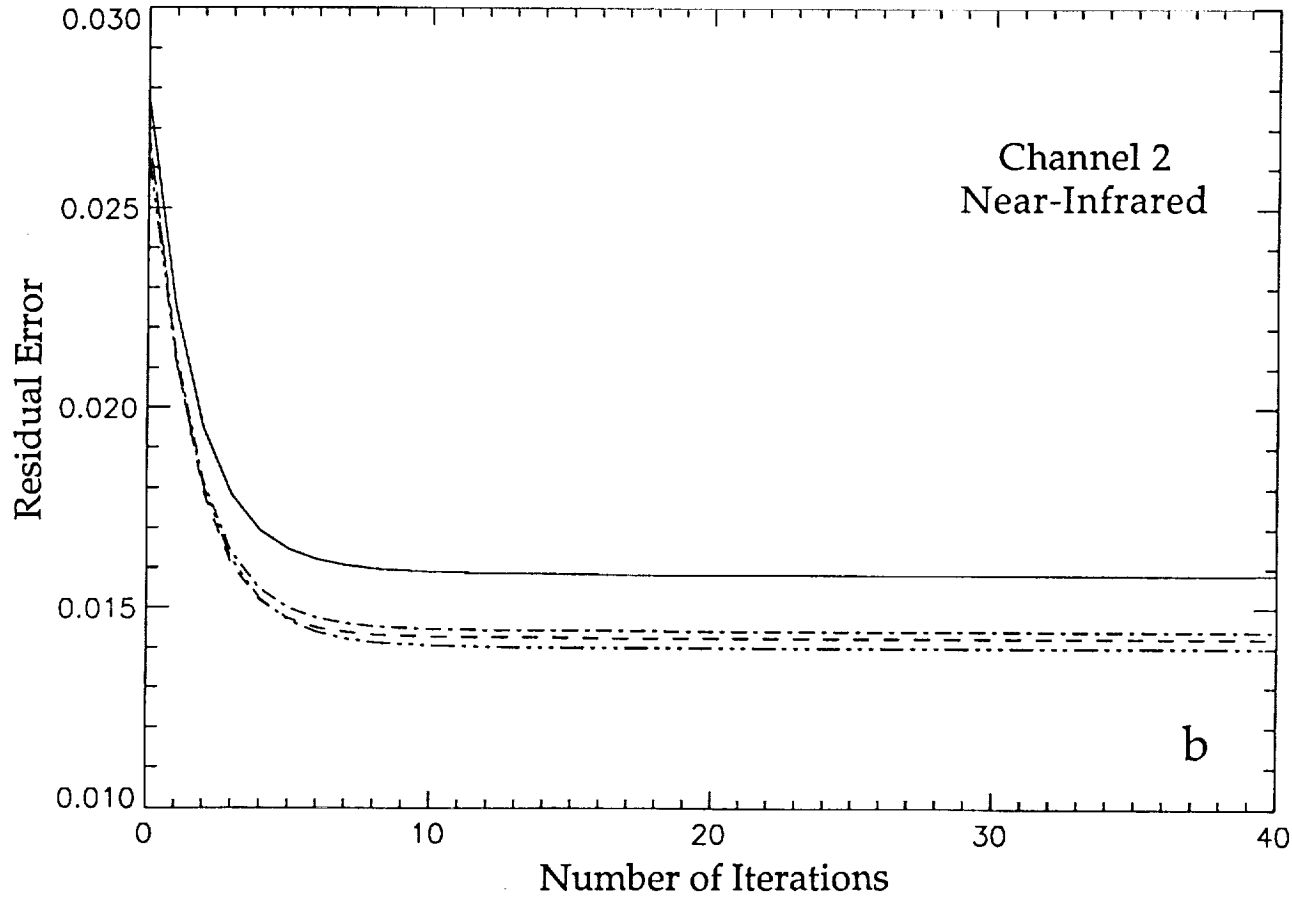

Fig. 9. Residual error between NOAA-9 AVHRR reflectance model and observations as a function of algorithm iterations . (a) channel 1 (visible); (b) channel 2 (near-infrared). The various curves correspond to the numbers of harmonics used to describe F, 4 to 7.

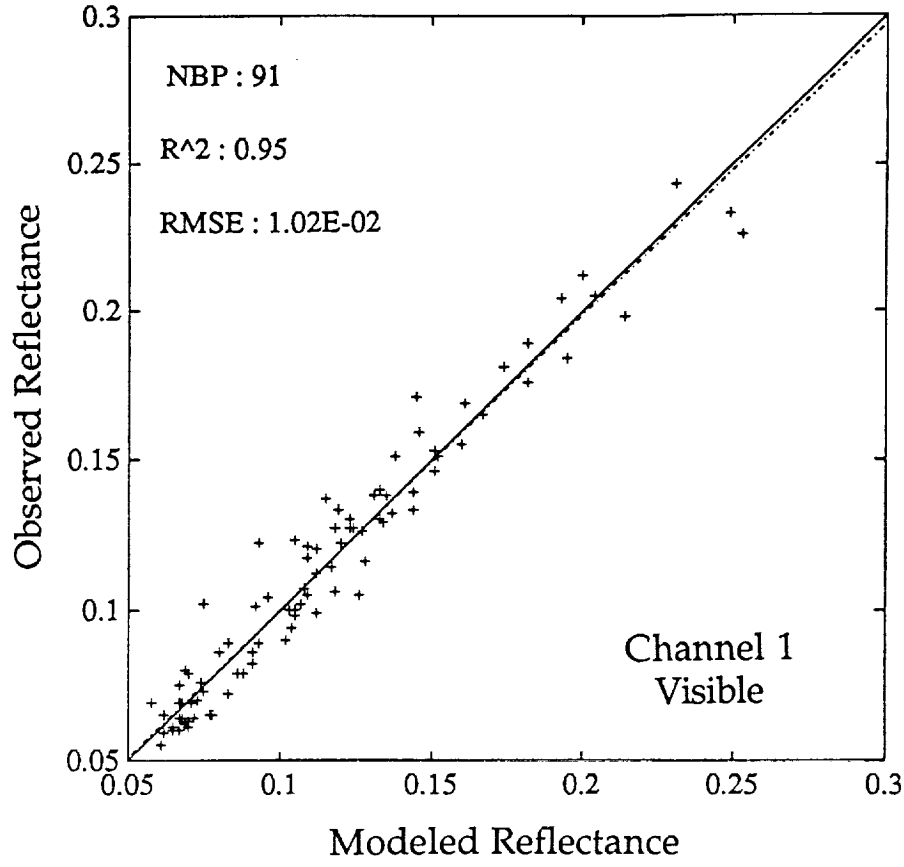

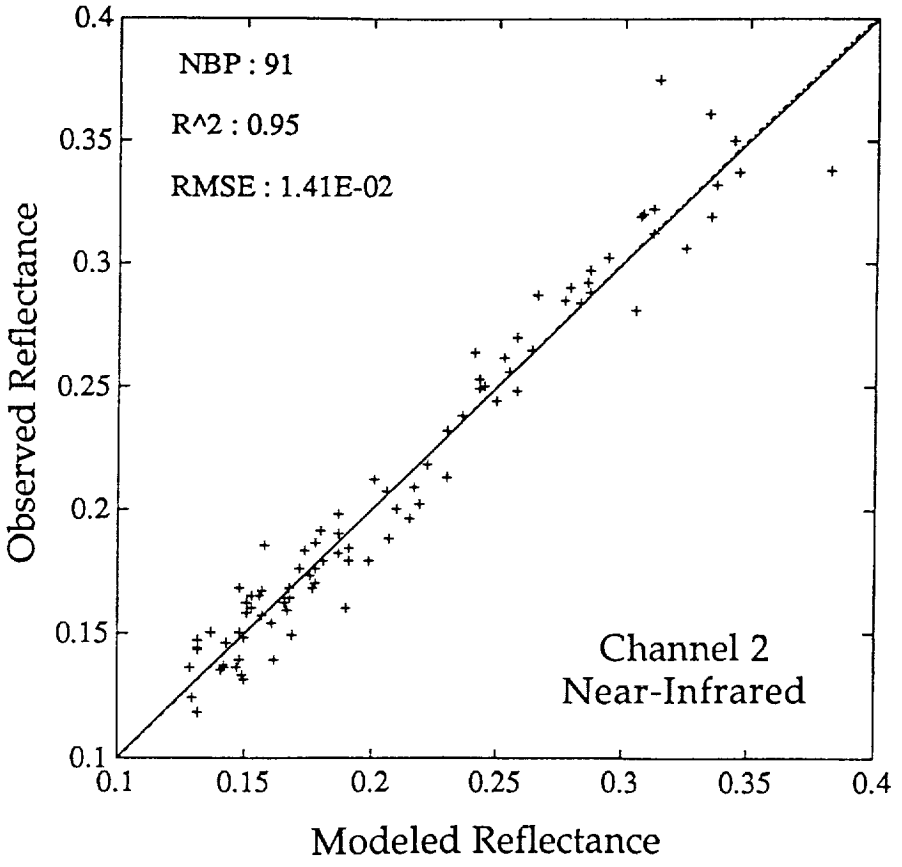

Fig. 10. Observed versus modeled NOAA-9 AVHRR reflectances. (Top) channel 1 (visible); (Bottom) channel 2 (near-infrared). Five harmonics are used to describe F.

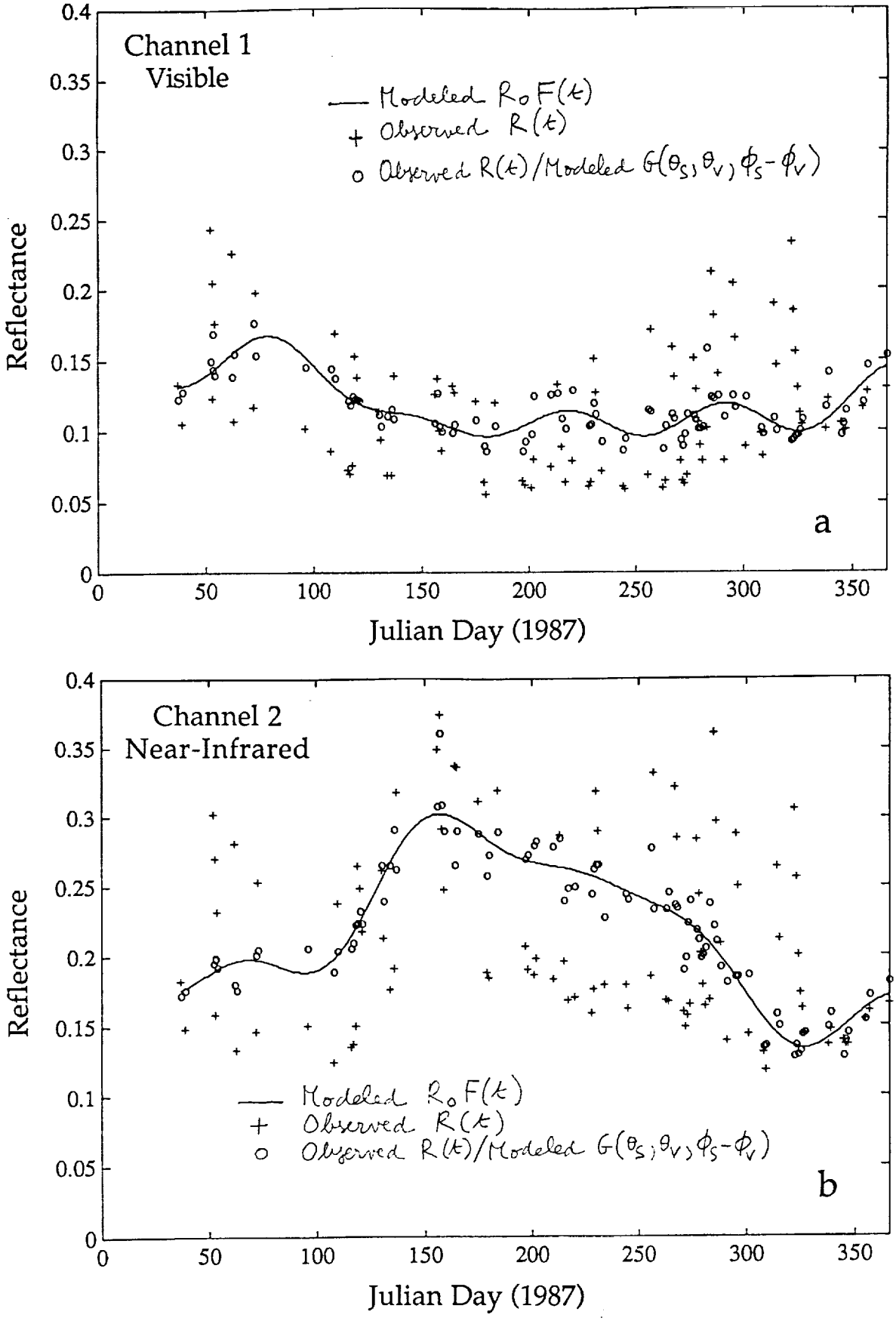

Fig. 11. Time series of modeled $R_0F(t)$, observed R(t), and observed R(t) normalized by $G(\theta_s,\theta_v, \phi_s-\phi_v)$ over the FIFE site during 1987. Satellite sensor is NOAA-9 AVHRR. (a) channel 1 (visible); (b) channel 2 (near-infrared).

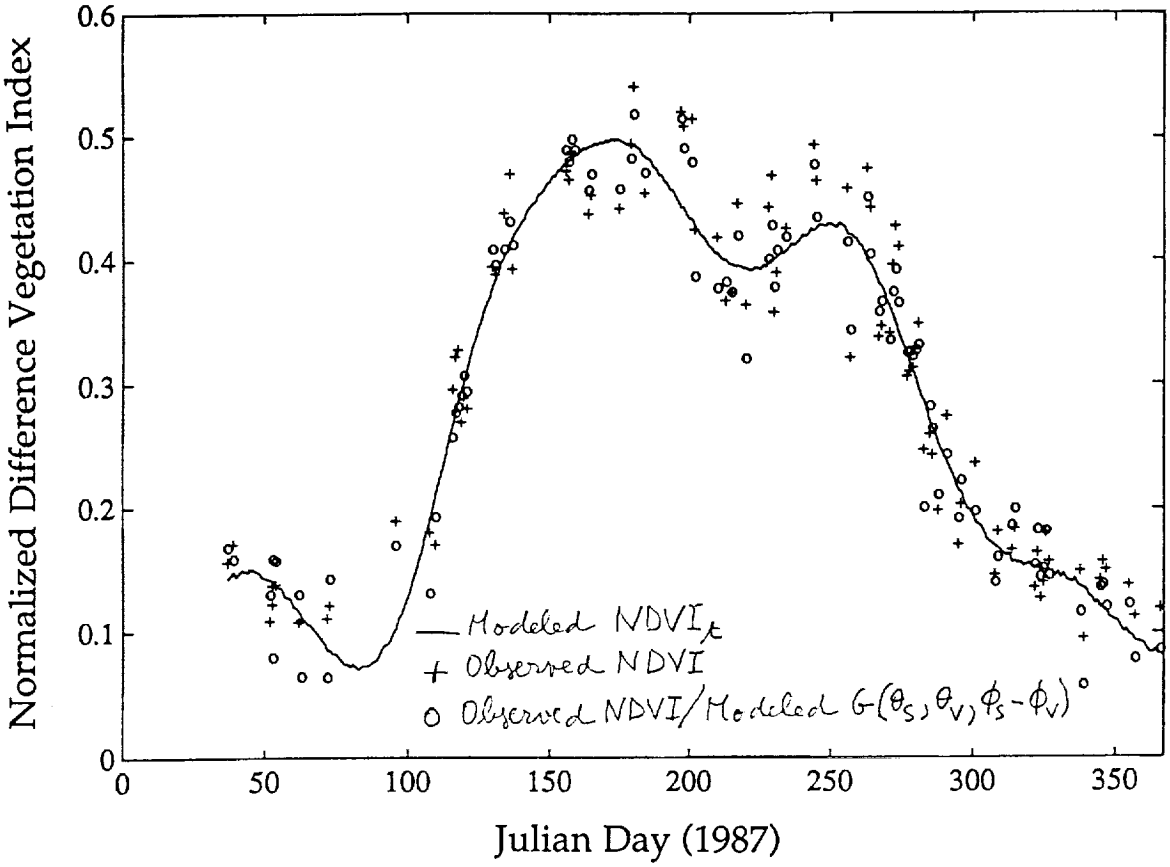

Fig. 12. Time series of Normalized Difference Vegetation Index calculated from modeled $R_oF(t)$, $NDVI_t(t)$, observed NDVI(t), and observed NDVI(t) normalized by $G(\theta s, \theta v, \phi s - \phi v)$ over the FIFE site during 1987. Satellite sensor is NOAA-9 AVHRR.

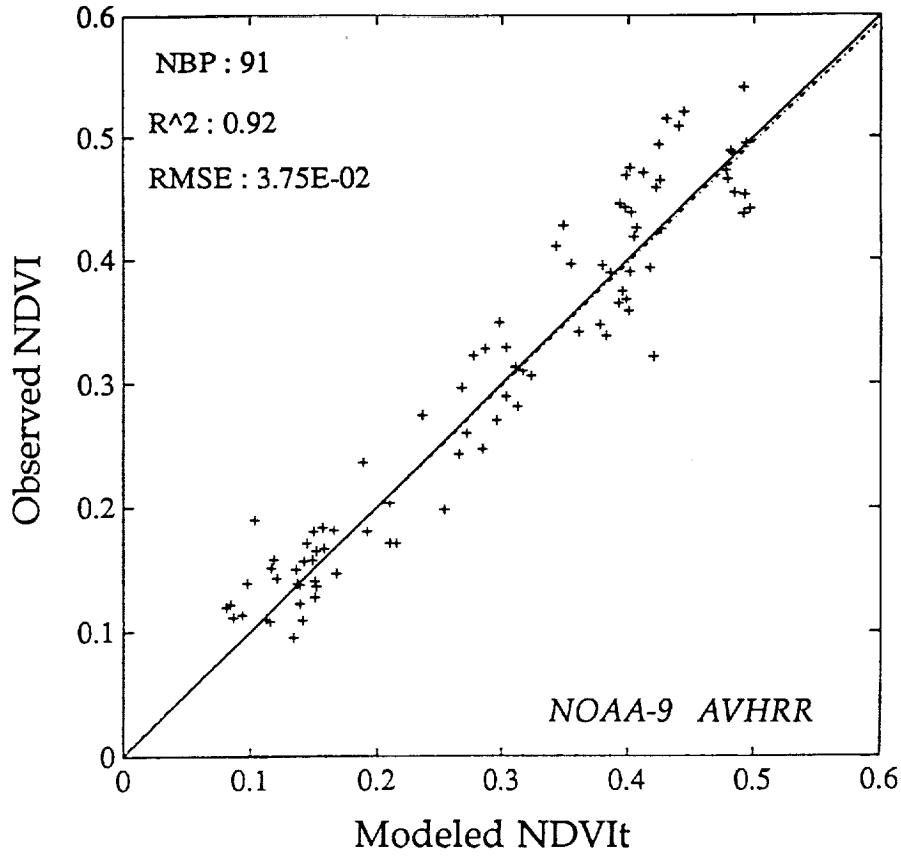

Fig. 13. Observed Normalized Difference Vegetation Index, NDVI, versus Normalized Difference Vegetation Index calculated from modeled $R_O F(t)$, $NDVI_t$.

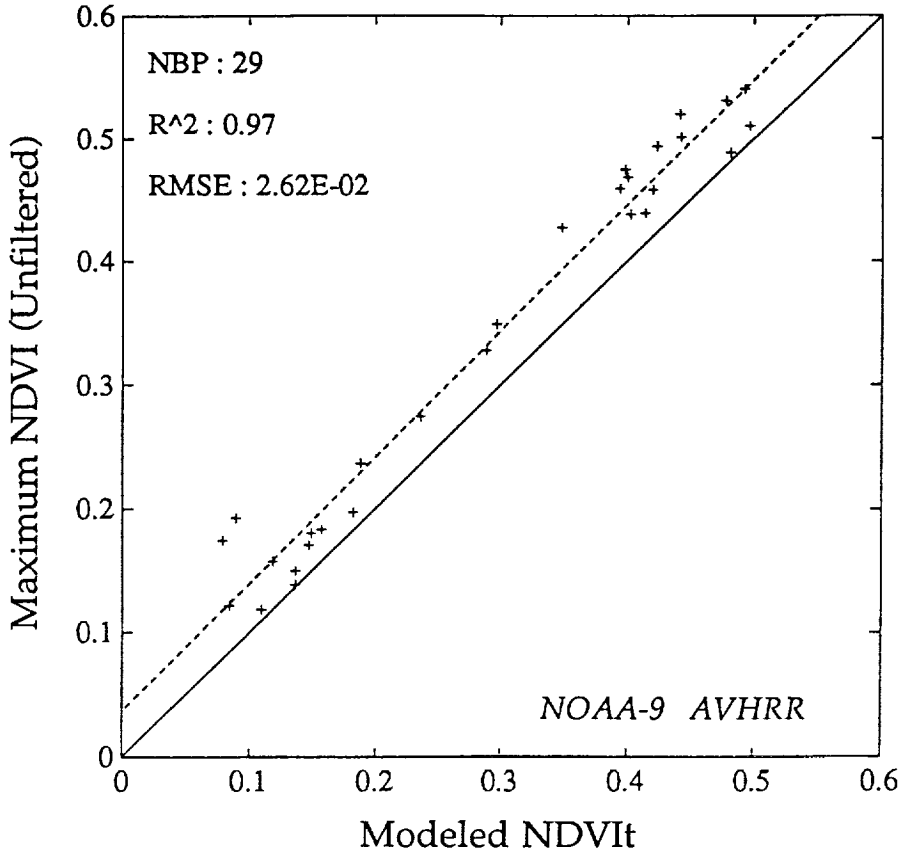

Fig. 14. Maximum Normalized Difference Vegetation Index over 11-day periods versus Normalized Difference Vegetation Index calculated from modeled $R_0F(t)$.

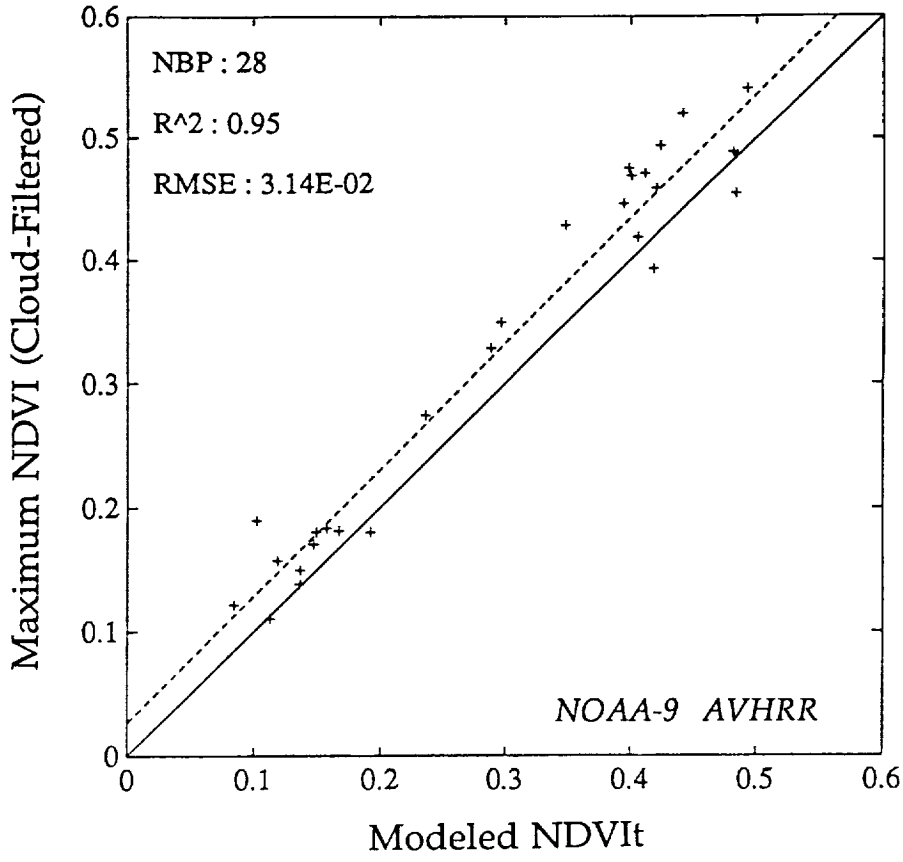

Fig. 15. Maximum Normalized Difference Vegetation Index over 11-day periods (after cloud-filtering) versus Normalized Difference Vegetation Index calculated from modeled $R_oF(t)$.

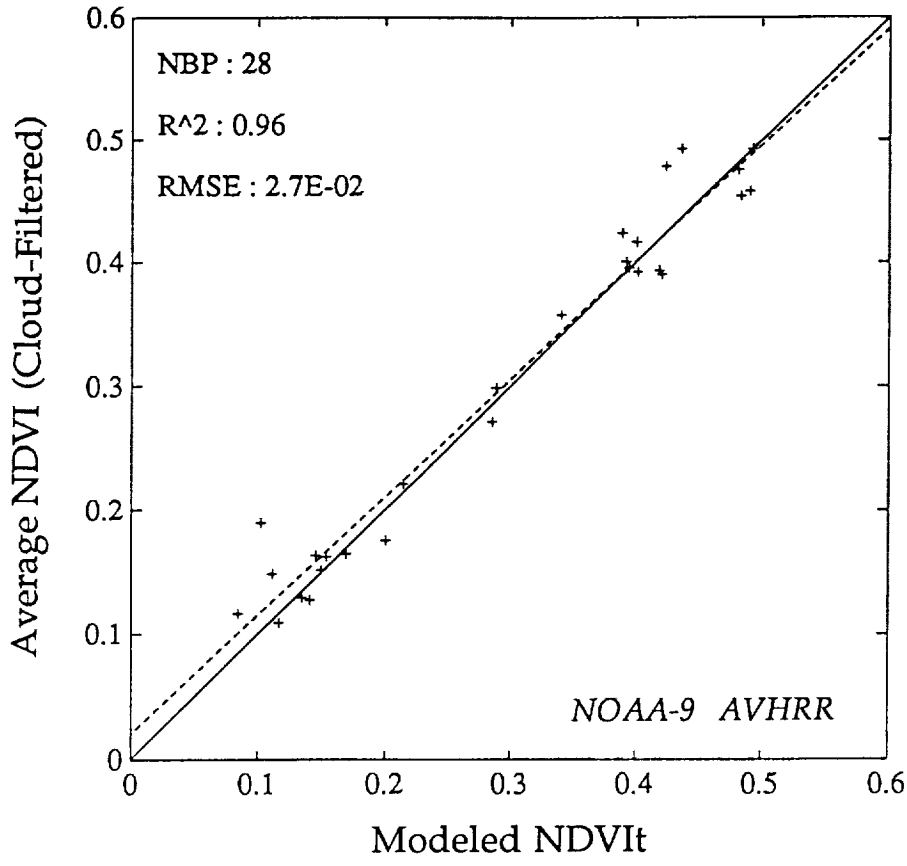

Fig. 16. Average Normalized Difference Vegetation Index over 11-day periods (after cloud-filtering) versus Normalized Difference Vegetation Index calculated from modeled $R_o F(t)$.

PREV. ANN

92N11474

Appendix 1

Optimum Combinations of Visible and Near-Infrared Reflectances for Estimating the Fraction of Photosynthetically Available Radiation Absorbed by Plants

A. Podaire, P.-Y. Deschamps, R. Frouin, G. Asrar

(Proceedings of the 5th International Colloquium-Physical measurements and signatures in Remote Sensing, Courchevel, France, 14-18 January 1991. ESA SP-319, 405-408, May 1991. Published by the European Space Agency)

OPTIMUM COMBINATIONS OF VISIBLE AND NEAR-INFRARED REFLECTANCES FOR ESTIMATING THE FRACTION OF PHOTOSYNTHETICALLY AVAILABLE RADIATION ABSORBED BY PLANTS

A. Podaire[1], P.Y. Deschamps[2], R. Frouin[3], G. Asrar[4]

[1] Centre National d'Etudes Spatiales; [2] Laboratoire d'Optique Atmosphérique;
[3] California Space Institute, Scripps Institution of Oceanography;
[4] National Aeronautics and Space Administration

ABSTRACT

A useful parameter to estimate terrestrial primary productivity, that can be sensed from space, is the daily-averaged fraction of photosynthetically available radiation (PAR) absorbed by plants. To evaluate this parameter, investigators have relied on the fact that the relative amount of radiation reflected by a vegetated surface in the visible and near-infrared depends on the fraction of the surface covered by the vegetation and, therefore, correlates with absorbed PAR. They have used vegetation indices, namely normalized difference and simple ratio, to derive absorbed PAR, even from coarse spatial resolution sensors such as the Advanced Very High Resolution Radiometer (AVHRR) aboard the NOAA satellites. The problem with normalized difference and simple ratio is first, they are non-linear functions of radiance or reflectance and, therefore, cannot be readily applied to heterogenous targets, second, they are used in generally non-linear relationships, which make time-integrals of the indices not proportional to primary productivity, and third, the relationships depend strongly on the type of canopy and background. To remove these limitations, we propose linear combinations of visible and near-infrared reflectances at optimum (one or two) viewing zenith angles.

Keywords: radiation, plants, primary production.

1. INTRODUCTION

Land primary productivity, or the rate at which materials from the atmosphere and soils are accumulated into biomass through photosynthesis, is of great importance. The reasons are numerous and have been discussed extensively in the literature (see, for instance, Ref. 1). Basically, the major portion of human food is provided by plants growing over land. Land primary productivity also affects the environmental context in which man and societies develop. In addition to its key role in sustaining human populations and structuring communities, land primary productivity governs to a large extent the seasonal oscillations of atmospheric carbon dioxide and impacts the water and energy available to the atmosphere. Anthropogenic changes, such as those linked to the destruction of major vegetation systems, have potential implications on climate. If we are to truly understand the interactions between the terrestrial biosphere and the atmosphere and their effects on climate, we need to know the geographic distribution and temporal variability of land primary productivity over the globe.

To achieve this goal, satellite observations are essential. A promising technique for sensing primary productivity from space, at least in the case of light-limited situations, incorporates the fact that the growth rate of many plants is close to proportional to the rate at which radiant solar energy is absorbed by the foliage (Ref. 2):

$$PP = e f_{PAR} PAR \qquad (1)$$

where PAR is the incident photosynthetically active radiation, practically the solar radiation reaching the canopy in the 0.4-0.7μm spectral interval, f_{PAR} is the fraction of PAR intercepted by the canopy, and e is an efficiency factor for carbon fixation that depends slightly on plant type, temperature, and available soil water. For various canopies (mostly crops), e has been found to lie between 1.1 and 1.4 g C per M J of PAR (Ref. 3).

Photosynthetically active radiation represents a nearly constant fraction of total insolation (e.g. Ref. 4), and total insolation can be retrieved accurately from satellite observations (e.g., Refs. 5, 6, 7, 8). Direct satellite estimates of PAR can also be obtained, as recent studies demonstrate (e.g., Ref. 9).

The absorbed fraction of PAR can be estimated from vegetation indices, the most commonly used being simple ratio, SR and normalized difference, ND. These indices are defined by:

$$SR = \frac{R_N}{R_V} \qquad (2)$$

$$ND = \frac{R_N - R_V}{R_N + R_V} \qquad (3)$$

where R_V and R_N are upwelling radiances in the visible and near-infrared (for instance radiances in channels 1 and 2 of the Advanced Very High Resolution Radiometer aboard NOAA satellites), respectively. Instead of radiances, reflectances are also used. That SR and ND are sensitive to f_{PAR} results from the characteristic spectrum of sunlight reflected by leaves, which is distinct from that of sunlight reflected by soils. Chlorophyll pigments absorb a large fraction of the light which reaches them in the visible, but not in the near-infrared where scattering by the chloroplasts is effective. This is not the case of soils, whose reflectance increases more linearly with wavelength in the visible and near-infrared. It follows that the relative amount of radiation reflected by a vegetated surface in the visible and near-infrared depends on the fraction of the surface covered by vegetation and, therefore, correlates with f_{PAR}.

Several theoretical studies have predicted how SR and ND relate to f_{PAR} (e.g., Refs. 2, 10, 11, 12, 13). Kumar (Ref. 2) suggested a near-linear relationship between SR and f_{PAR}. Asrar et al. (Ref. 10) and Sellers (Refs. 11, 12) showed that f_{PAR} should vary non-linearly with SR, but almost linearly with ND. Choudhury (Ref. 13) found that the relationships between f_{PAR} and vegetation indices are generally non-linear. Soil reflectance changes, in particular, appeared to significantly affect the linearity of the relationships.

Experimental studies (e.g., Refs. 2, 14, 15, 16, 17) have also provided disparate results and, therefore, did not resolve the apparent theoretical controversy. Kumar (Ref. 2), for instance, observed that SR is linearly related to f_{PAR} for sugar beet, which supported their theoretical analysis, yet Steven et al. (Ref. 14) reported an exponential relationship. In short, the observations indicate that the relationships between f_{PAR} and vegetation indices depend strongly on the type of canopy and underlying surface, as pointed out by Choudhury (Ref. 13).

Proceedings of the 5th International Colloquium – Physical Measurements and Signatures in Remote Sensing, Courchevel, France, 14–18 January 1991 (ESA SP-319, May 1991).

That the interdependence of f_{PAR} and vegetation indices is linear or non-linear is an important issue because linearity implies that the time-integral of SR and ND should also be linearly related to primary production (e.g., Refs. 11, 12, 18). Even though serious doubts exist about the linearity of the relationships, especially when considering various ecosystems and climates, Tucker et al. (Ref. 19) and Goward et al. (Refs. 20, 21) have reported agreement between ND time-integrals obtained from AVHRR data over the Senegalese Sahel and North and South American biomes, respectively, and published production rates.

Using SR or ND for estimating f_{PAR}, has several limitations. First, as mentioned above, the relationships are generally non-linear, which makes SR and ND time-integrals not proportional to primary production. Second, SR and ND are non-linear functions of radiance. Since vegetation is highly heterogeneous spatially, sub-pixel variability is likely to introduce uncertainties in SR and ND, particularly when the sensor spatial resolution is coarse (case of AVHRR). For such sensors, which have the advantage of frequent global coverage, applying relationships established for homogeneous canopies is not satisfactory. Third, satellite-derived SR and ND may reduce to some extent the effects of sensor calibration uncertainties and atmospheric interference, yet they depend on atmospheric composition, in particular aerosol and water vapor amounts, and viewing geometry (e.g., Ref. 22). Even time series of maximum AVHRR vegetation indices over a several-day period, which correspond to minimum atmospheric contamination, remain relatively noisy, and it has not yet been possible to identify whether the noise is due to residual variations in the atmospheric contribution or to variable directional surface properties. We need to address these limitations if we are to remotely sense f_{PAR} from space accurately .

Our objective, therefore, and the purpose of this paper, is to define optimum combinations of visible and near-infrared reflectances that: a) relate linearly to f_{PAR}; b) can be used independently of the type of foliage and substrate; c) eliminate the effects of sub-pixel spatial heterogeneity; and d) improve the accuracy of f_{PAR} estimates when compared to SR and ND.

2. METHODOLOGY

Instead of using radiance ratios, we express f_{PAR} as a linear combination of visible and near-infrared radiances or, equivalently, reflectances. This procedure, when applied to a coarse resolution sensor such as AVHRR, should eliminate or, at least, substantially reduce sub-pixel variability effects. Linear combinations of reflectances, known as "greenness" transformations, have been used for many years to study vegetation parameters, in particular by Hatfield et al. Ref. 15) and Asrar et al. (Ref. 17). These authors found that greenness obtained by combining reflectances measured by a Barnes Modular Multispectral Radiometer (MMR) in two visible and two near-infrared bands is a much more linear predictor of f_{PAR} than simple ratio and normalized difference. They did not favor greenness, however, because of the smaller sensitivity of this index to f_{PAR} and the strong dependence of the relationship between f_{PAR} and greenness upon solar zenith angle and canopy geometry. If known (e.g., from theoretical calculations), the dependence upon solar angle or, more generally, radiation geometry, should not be a problem because solar and viewing angles can be determined exactly. The problem is to eliminate the effects of variable canopy geometry and soil reflectance in the relationships. Given a sun position, this may be possible for specific viewing angles.

Our approach, therefore, is to simulate for varied soil and canopy parameters, namely leaf optical properties, soil reflectance, leaf area index (LAI), and leaf inclination distribution function (LIDF), above-canopy visible and near-infrared reflectances as well as f_{PAR} and daily averaged (weighted by incident radiation) f_{PAR}, $\overline{f_{PAR}}$. The simulations are performed which the SAIL canopy reflectance model (Ref. 23). Various radiation geometries (solar and viewing zenith angles, relative azimuth angle) are considered, as well as direct and diffuse fractions of incident solar radiation. The absorbed fraction of PAR, f_{PAR}, is computed as a function of solar zenith angle and $\overline{f_{PAR}}$ as a function of latitude and season. From the reflectances, simple ratio and normalized difference are derived.

We focus on $\overline{f_{PAR}}$ since this parameter rather than f_{PAR} is required in primary productivity models. In addition, since the sensors potentially useful to monitor land primary productivity from space are, or will be carried by heliosynchronous satellites (AVHRR on the NOAA series, the POLarization and Directionality of the Earth Reflectance instrument, POLDER, on ADEOS, and the MODerate resolution Imaging Spectrometer, MODIS, on EOS) and, therefore, offer the possibility of viewing the same target under one or several geometries during a several-day period, we attempt to estimate $\overline{f_{PAR}}$ from single or multi-angle combinations of visible and near-infrared reflectances. Indeed, the multi-angle approach is only suitable when the characteristics of the surface target do not change significantly over the several-day period.

Thus, we regress $\overline{f_{PAR}}$ at each latitude and month during the year against simple ratio, normalized difference, and visible and near-infrared reflectances. One and two viewing geometries are considered for the combinations of reflectances. The regression statistics, namely correlation coefficient, regression coefficients, and residual error of estimate are analyzed to determine the solar and viewing angles that minimize the effects of variable LIDF and soil reflectance. The improvement in the predicting power of the linear combinations is also assessed.

3. RESULTS

To illustrate our theoretical approach and show the promise of linear combinations, Figs. 1, 2, and 3 display selected results obtained with the SAIL model. The calculations were performed for LAIs of 0.01, 0.05, 0.1, 0.2, 0.5, 1, 2, and 5, erectophile, spherophile, and planophile canopies, soil reflectances of 0.1, 0.2, 0.3, and 0.4, and typical leaf optical properties (reflectance and transmittance of 0.1 and 0.001, respectively, in the visible, and 0.45 and 0.4 in the near-infrared). The soil reflectance was assumed white spectrally, and the various LIDFs were considered conjointly in the regressions. A US 62 standard atmosphere (Ref. 24) containing continental aerosols (Ref. 25) was overlying the canopy. We see in Fig. 1 (bottom) that the influence of the background on the $\overline{f_{PAR}}$ versus ND relationships is substantial, especially at moderate LAIs, but is reduced considerably when using linear combinations of reflectances (Fig. 2, bottom). In this case, the points corresponding to a same LAI are generally more aligned with the best fit line. The result is a drastic improvement in the $\overline{f_{PAR}}$ residual error. For the solar and viewing geometries of Figs. 1 and 2 ,bottom, the residual error is reduced from 0.058 to 0.033. When using ND the minimum residual error is obtained for a nadir viewing (Fig. 1, top), but when using linear combinations it is preferable to view the canopy at a 45° zenith angle (Fig. 2, top). The $\overline{f_{PAR}}$ residual error can be further reduced by combining linearly visible and near-infrared reflectances at two viewing zenith angles (Fig. 3). Using reflectances at nadir and 60° from zenith, for instance, reduces the $\overline{f_{PAR}}$ residual error to 0.026 (Fig. 3, bottom). Smaller residual errors can even be obtained when the second viewing zenith angle is as far as possible from nadir (Fig. 3, top).

The above results, however, are only valid for a sun at 60° of zenith in July and at 45° latitude. For a sun closer to zenith, the minimum $\overline{f_{PAR}}$ residual error is encountered at higher viewing zenith angles when using ND, for instance at 45° when the sun is at 30° from zenith. In the case of uni-angle linear combinations, the minimum at 45° (Fig. 3, top) moves to 60° when the sun zenith angle decreases to 30°. The picture is more complex with multi-angle combinations because of the many angular possibilities. In general, for a particular sun configuration, several viewing zenith angle pairs provide similar good results ($\overline{f_{PAR}}$ residual error around 0.020). For a sun at 30° from zenith, for instance, viewing at nadir, 15°, or 30° from zenith and at 75° from zenith gives residual errors ranging from 0.019 to 0.021. The regression coefficients, however, are quite sensitive to the viewing geometries selected.

4. DISCUSSION

The results presented in section 3, although encouraging, should be interpreted with caution. No hasty generalization can be made at this point. First, the SAIL model has often showed weaknesses when compared to measurements; it does not predict a hot spot and is only appropriate for agricultural plants that form a layer-type canopy. More accurate canopy reflectance models may be used, at least to provide a reference. Second, the background reflectance

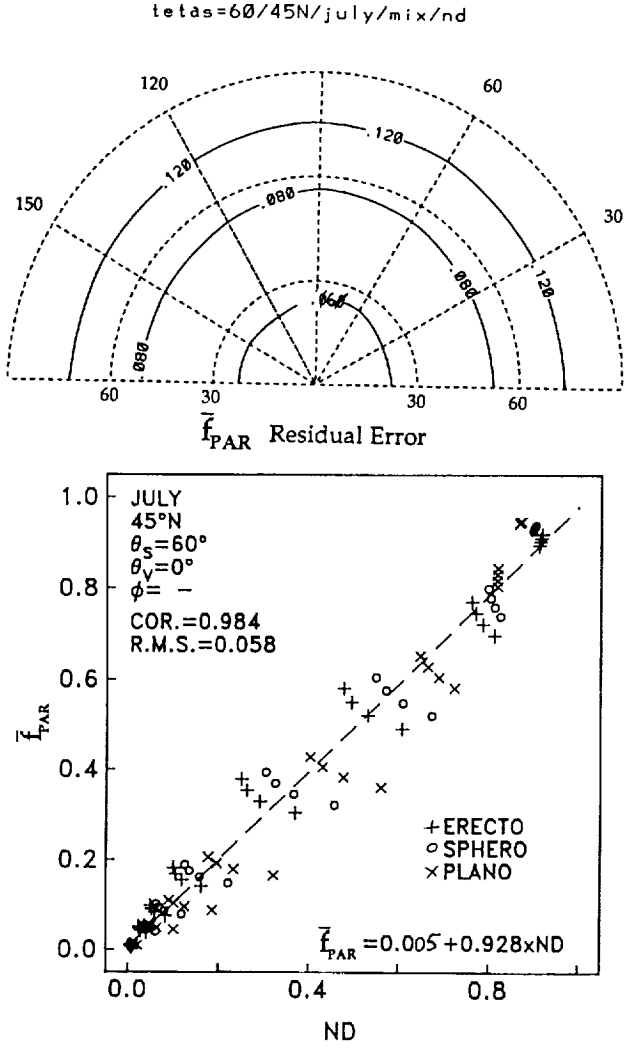

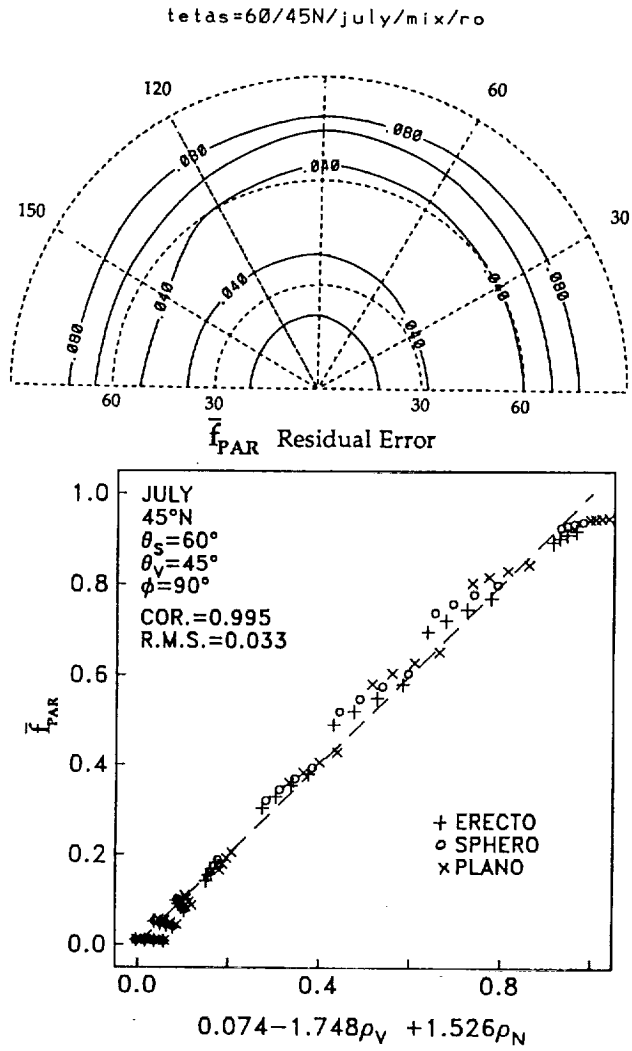

Fig. 1 Top: $\bar{f}_{PAR}$ residual error as a function of viewing geometry for a sun at 60° from zenith in July at 45°N. In the calculations, $\bar{f}_{PAR}$ estimated from normalized difference, ND, is compared to $\bar{f}_{PAR}$ obtained with the SAIL model. Bottom: scatter plot of $\bar{f}_{PAR}$ versus ND for a nadir viewing. Variable soil reflectance results in points aligned rather perpendicularly to the best fit line (dashed line), especially at moderate LAIs $\bar{f}_{PAR}$ and ND values around 0.5), which indicates that the relationship between $\bar{f}_{PAR}$ and ND is not only non-linear, but also strongly depends on the type of background.

Fig. 2 Same as Fig. 1, but linear combinations of visible and near-infrared reflectances (single viewing geometry), ρ_V and ρ_N, respectively. Compared to Fig.1, the $\bar{f}_{PAR}$ residual error is substantially reduced when viewing around 45° from zenith. Points corresponding to a same LAI, but different soil reflectances, are now more aligned along the best fit line.

may vary with wavelength in the visible and near-infrared, as is the case with most soils (e.g., Ref. 27) and leaf litter (Ref. 28). The canopy may also be composed of living as well as dead leaves or, more generally, leaves of different optical properties. Calculations, therefore, should include more realistic situations. Still, our study strongly suggests that linear combinations at specific viewing angles may be much more accurate in predicting $\bar{f}_{PAR}$ than indices that are non-linear functions of radiances or reflectances.

The relationships established theoretically, the gain in $\bar{f}_{PAR}$ residual error when using preferential viewing geometries, the ability of the linear combinations to reduce soil and LIDF dependence, etc., remain to be verified using in situ measurements. Unfortunately, few data sets exist that contain concomitant $\bar{f}_{PAR}$ and reflectance measurements at various viewing angles. The results, therefore, may not be statistically significant. A dedicated experiment to establish and verify the validity of the SAIL-based data fits, therefore, appears necessary.

One should further emphasize that surface reflectances observed from space are inherently subjected to instrument noise and are contaminated by the atmosphere. Consequently, it will be necessary in the comparisons of the various estimators' performance to include the effects of instrument noise and atmospheric interference, which act differentially on simple ratio, normalized difference, and linear combinations. This can be done by simulating the top of atmosphere reflectances corresponding to the surface reflectances, correct those reflectances for atmospheric effects assuming typical atmospheric characteristics, and translate the effects of uncertainties in these characteristics into above-canopy reflectance uncertainties. The procedure is then to introduce the above canopy reflectance uncertainties in the regression datasets, as well as typical instrument noise.

Our investigation should be viewed in the context of future spaceborne radiometers, in particular MODIS on EOS and POLDER atmosphere reflectances for atmospheric interference, are particularly adapted to monitor $\bar{f}_{PAR}$ and, therefore, primary productivity from linear (uni- and multi-angle) combinations of reflectances. This should lead, during the EOS era, to a better characterization of terrestrial primary productivity on a global scale.

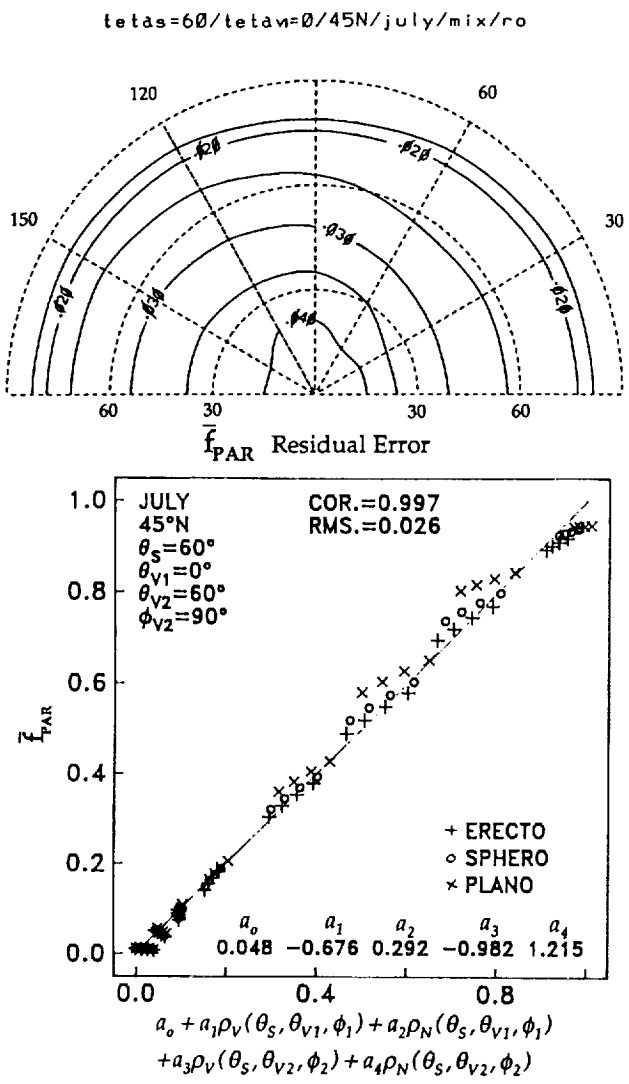

Fig. 3 Same as Fig. 2, but two viewing geometries. Compared to Fig. 2, the f_{PAR} residual error is further reduced when reflectances at nadir and 60° from zenith are linearly combined.

5.ACKNOWLEDGMENTS

This work has been supported by the National Aeronautic and Space Administration under grants NAG5-900 and NAGW-1968 and by the California Space Institute under grant CS76-90. We wish to thank F. Hall, K. Huemmrich, and E. Middleton of NASA Goddard Space Flight Center and B. Blad and E. Walter-Shea of the University of Nebraska for helpful discussions, M. Ba for technical support.

6. REFERENCES

1. Lieth H., 1975: Modeling the primary productivity of the world. *In "Primary productivity of the biosphere"* H. Lieth and R.H. Whittaker eds. Springer-Verlag New York/Heidelberg/ Berlin.

2. Kumar, M. and J.L. Monteith, 1981: Remote sensing of crop growth. *In "Plants and Daylight Spectrum"*, H. Smith, Ed., Academic, New York, 133-144.

3. Monteith, J. L., 1977: Climate and the efficiency of crop production in Britain. *Phil. Trans. Roy. Soc. London*, B281, 277-294.

4. Baker, K. S. , and R. Frouin, 1987: Relation between photosynthetically available radiation and total insolation at the ocean surface under clear skies. *Limnol. Oceanog.*, 32, 1370-1377.

5. Tarpley, J. D., 1979: Estimating incident solar radiation at the surface from geostationary satellite data. *J. Appl. Meteor.*, 41, (4), 1172-1181.

6. Gautier, C. G. Diak and S. Masse, 1980: A simple physical model to estimate incident solar radiation at the surface from GOES satellite data. *J. Appl. Meteor.*, 19, 1005-1012.

7. Pinker, R. T. , and J.A. Ewing, 1985: Modeling surface solar radiation: Model formulation and validation. *J. Clim. and Appl. Meteor.*, 24, (5), 389-401.

8. Dedieu, G., P. Y. Deschamps and Y.H. Kerr, 1987: Satellite estimation of solar irradiance at the surface of the earth and of surface albedo using a physical model applied to Meteosat data. *J. Clim. and Appl. Meteor.*, 26, (1), 79-87.

9. Frouin, R. and C. Gautier, 1990: Variability of photosynthetically available and total solar irradiance at the surface during FIFE. *Symposium on the First ISLCP Experiment-FIFE*, Feb. 7-9, 1990 Anaheim, CA,

10. Asrar, G. M. Fuchs, E.T. Kanemasu and J.L. Hatfield, 1984: Estimating absorbed photosynthetic radiation and leaf area index from spectral reflectance in wheat. *Agron. J.*, 6, 300-306.

11. Sellers, P. J., 1985: Canopy reflectance, photosynthesis and transpiration. *Int. J. Rem. Sens.*, 6, 1335-1372.

12. Sellers, P. J., 1987: Canopy reflectance, photosynthesis, and transpiration. II. The role of biophysics in the linearity of their interdependence. *Rem. Sens. Environ.*, 21, 143-183.

13. Choudhury, B. J., 1987: Relationships between vegetation indices, radiation absorption, and net photosynthesis evaluated by a sensitivity analysis. *Rem. Sens. Envir.*, 22, 209-233.

14. Steven, M. D. , P.V. Biscoe, and K.W. Jaggard, 1983: Estimation of sugar beet productivity from reflection in the red and infrared spectral bands. *Int. J. Remote Sens.*, 4, 325-334.

15. Hatfield, J. L. , G. Asrar, and E.T. Kanemasu, 1984: Intercepted photosynthetically active radiation estimated by spectral reflectance. *Remote Sens. Environ.*, 14, 65-75.

16. Gallo, K. P. , C.S.T. Daughtry, and M.E. Bauer, 1985: Spectral estimation of absorbed photosynthetically active radiation in corn canopies. *Remote Sens. Envir.*, 17, 221-232.

17. Asrar, G. E. T. Kanemasu, G.P. Miller, and R.L. Weiser, 19887: Light interception and leaf area estimates from measurements of grass canopy reflectance.(IEEE). *Trans. Geosciences and Remote Sensing*, GE-24, 76-82.

18. Tucker, C. J. , and P.J. Sellers, 1986: Satellite remote sensing of primary production. *Int. J. Remote Sensing*, 2, 1395-1416.

19. Tucker, C. J. , C.L. Vanpraet, M.J. Sharman and G. Van Ittersum, 1985: Satellite remote sensing of total herbaceous biomass production in the Senegalese Sahel: 1980-1984. *Remote Sens. of Environ.*, 17, 233-249.

20. Goward, S. N. , C.J. Tucker, and D.G. Dye, 1985: North American vegetation patterns observed with the NOAA-7 advanced very high resolution radiometer. *Vegetation*, 64, 3-14.

21. Goward, S. N. , D.G. Dye, A. Kerber, and V. Kalb, 1987: Comparison of north and south American biomes from AVHRR observations. *Geocarto International*, 1, 27-39.

22. Holben, B. N. , and R.S. Fraser, 1984: Red and near-infrared sensor response to offnadir viewing. *Int. J. Remote Sensing*, 5, 145-160.

23. Verhoef, W., 1984: Light scattering by leaf layers with application to canopy reflectance modeling: The SAIL model. *Rem. Sens. Environ.*, 16, 125-141.

24. Mc Clatchey, R.A., R.W. Fenn, J.E.A. Selby, F.E. Voltz, and J.S. Garing, 1971: Optical roperties of the atmosphere. AFCRL 71-0279, Environ, Res. Paper 354, 108 pp.

25. WCP-55, 1983: Report of WMO (CAS)/Radiation Commission of IAMAP Meeting of Experts on Aerosols and their Climatic Effects, Williamsburg, Virginia, March 28-30, 1983.

26. Stoner,E.R., and M.F. Baumgardner, 1981: Characteristic variations in reflectance of surface soils, *Soil Sci. Soc. Am. J.* ,45(6), 1161-1165.

27. Hall, F.G., and K.F. Huemmrich, 1990: Use of narrow-band spectra to estimate the fraction of absorbed photosynthetically active radiation. *Remote Sens. Environ.*, 29, 47-53.

PREV. ANN.
92A 42287

Appendix 2

Upscale Integration of Normalized Difference Vegetation Index: The Problem of Spatial Heterogeneity

A. Aman, H. P. Randriamanantena, A. Podaire, and R. Frouin
(IEEE Transactions on Geoscience and Remote Sensing, Vol. 30, No. 2, 326-338, March 1992)

Upscale Integration of Normalized Difference Vegetation Index: The Problem of Spatial Heterogeneity

Angora Aman, Heremino P. Randriamanantena, Alain Podaire, and Robert Frouin

Abstract—**Spatial integration of radiometric parameters that describe the Earth's vegetation cover is an important issue ~~important~~ when studying global scale land–atmosphere interactions. The Normalized Difference Vegetation Index (NDVI) is currently used to characterize the land surface in terms of vegetation cycles and primary production. The NDVI is sensitive to fractional vegetation cover, canopy density, leaf architecture, and leaf physical state. A potential problem with NDVI, however, is that it does not depend linearly on radiance or reflectance. Since vegetation can be highly heterogenous spatially, and since the relationships between NDVI and vegetation parameters are established locally, using NDVI derived from coarse resolution sensors such as NOAA Advanced Very High Resolution Radiometer (AVHRR) may not be appropriate. The purpose of this paper, therefore, is to analyze the correspondence between NDVI calculated from average reflectances, M_{NDVI}, and NDVI integrated from individual NDVI's, I_{NDVI} by simulating AVHRR data from high spatial resolution SPOT 1 Haute Résolution Visible (HRV) radiometer and Landsat Thematic Mapper (TM) data. For the considered sites, located in tropical West Africa and temperate France, and the scales analyzed, 300–1000 m, a strong correlation exists between the two types of index. The relationship is almost perfectly linear, with a slope depending slightly on the variability of the vegetation cover. Effecting the scale change using M_{NDVI} instead of I_{NDVI} does not introduce significant errors, especially when these errors are compared to those resulting from uncertainities in the relationships between NDVI and vegetation parameters, which are typically one order of magnitude higher. Other sites should be examined, however, and the variability within TM and HRV Radiometer pixels quantified in order to conclude definitely and generally about the adequacy of using M_{NDVI} in parameterizations obtained at the local scale.**

I. Introduction

Global monitoring of the earth's vegetation cover is important to understand land–atmosphere interactions and their effects on climate. This has been identified as a major task of the International Geosphere-Biosphere Program (IGBP) and its space component, the Earth Observing System (EOS) (see [1], [2]). Changes in land use and, hence, vegetation cover, directly impact surface water and energy budgets through plant transpiration, surface albedo, emissivity, and roughness. They also affect primary production and, therefore, the global carbon cycle. Since atmospheric carbon dioxide (CO_2) concentration is mainly regulated by primary production, at least on a seasonal or annual time scale, characterizing vegetation dynamics is crucial to assessing the fate of the current increase in atmospheric CO_2.

Satellites can provide a spatially comprehensive view of land vegetation cover. The time frequency of the data, however, may not be adequate to monitor phenological changes. This is the case of data from high spatial resolution sensors, such as the LANDSAT Thematic Mapper (TM) and the SPOT Haute Résolution Visible (HRV) radiometer, which have repetitive cycles of 16 and 26 days, respectively. Studies of vegetation dynamics, therefore, have been carried out using higher time frequency data from sensors with coarser spatial resolution, namely, the Advanced Very High Resolution Radiometer (AVHRR) aboard the NOAA satellites.

The spatial resolution of AVHRR images (about 1.1 km at nadir) has been shown to be sufficient for investigating vegetation changes on subcontinental to global scales (e.g., [3]). However, because vegetation is highly variable spatially, a system with at least 500 m resolution will offer major benefits when compared to 1.1 km resolution system ([3], [4]).

The AVHRR provides data in visible, near-infrared, and thermal infrared regions of the electromagnetic spectrum. There is a strong absorption of incident solar radiation by chlorophyll pigments in the visible, while scattering by the chloroplast in the near-infrared region leads to high reflectance values. Consequently, the Simple Ratio (SR) or the Normalized Difference Difference Vegetation Index (NDVI), which both exploit the differential reflectance properties of plants in the visible and near-infrared, have been used largely to monitor land vegetation.([5], [6]) The SR and NDVI are defined by:

$$SR = NIR/VIS \tag{1}$$

$$NDVI = (NIR - VIS)/(NIR + VIS) \tag{2}$$

where NIR and VIS are satellite radiances or reflectances

Manuscript received September 26, 1991; revised November 1, 1991.This research has been funded by the Centre National d'Etudes Spatiales and the Centre National de la Recherche Scientifique, France, the National Aeronautics and Space Administration under grant NAGW-1968, and the California Space Institute. A. Aman received support from the Ministère de la Recherche Scientifique of Ivory Coast.

H. P. Randriamanantena is with the Laboratoire dEtudes et de Recherches en Télédétection Spatiale, 18 Avenue Edouard Belin, 31055 Toulouse cédex, France.

A. Aman and A. Podaire were with the Laboratoire dEtudes et de Recherches en Télédétection Spatiale. A. Aman is now with the Département de Physique, Faculté des Sciences, 22BP522 Abidjan 22, Ivory Coast.

A. Podaire is with the Centre National dEtudes Spatiales, RE/SU/TE, 18 Avenue Edouard Belin, 31055 Toulouse cédex, France.

R. Frouin is with the California Space Institute, Scripps Institution of Oceanography, La Jolla, CA 92093-0221.

IEEE Log Number 9105386.

in the near-infrared and visible, respectively. The SR and NDVI depend on vegetation parameters such as leaf greenness, fraction of vegetation cover, soil type, soil moisture (e.g., [7]), and these parameters vary according to climatic conditions. Maps of vegetation physical properties derived from SR or NDVI may be used as inputs into local, medium, or global scale models. It is highly desirable, therefore, to map them at compatible spatial scales. Using AVHRR-derived SR and NDVI, however, may not be appropriate because these indexes are nonlinear functions of radiances or reflectances. Since vegetation can be highly heterogeneous spatially, subpixel variability is likely to introduce uncertainities in SR and NDVI.

In this paper, we address the problem of spatial integration of NDVI. For a given area, linear regressions are performed between mean and integrated NDVI's calculated from high spatial resolution data (HRV radiometer and TM). Mean NDVI is obtained from visible and near-infrared reflectances averaged over the area, whereas integrated NDVI is obtained by averaging all NDVI's within the area. The scales considered range from 300 to 1000 m; they correspond roughly to the spatial resolution of present and future sensors dedicated to or suitable for large-scale vegetation studies.We discuss the influence of spatial heterogeneity and structure of the reflectance fields on the slope of the linear regressions. The results are presented for the Sudano-sahelian zone as well as temperate agricultural sites in France.

II. Background

Spatial integration of vegetation indices is necessary to study net primary production and land–atmosphere interactions at the global scale. The physical processes characterizing vegetation are often difficult to describe and are generally parameterized at the local scale using field measurements. The problem is to extend these parameterizations to larger scales when taking vegetation into consideration within Global Circulation Models (GCM's).

Many studies, experimental as well as theoretical, have shown that primary production depends on the fraction of photosynthetically active radiation intercepted by plants, or IPAR. Experimental measurements, on the one hand, suggest that IPAR depends linearly on NDVI ([8], [9]). Theoretical considerations, on the other hand, indicate that for IPAR values beyond 0.6 the relationship is highly curvilinear (e.g., [10], [11]). Therefore, the hypothesis of a linear relationship between NDVI and IPAR only holds for specific vegetation situations (e.g., well-mixed area, partially covered by vegetation).

Another important parameter used to characterize vegetation structure or architecture is the Leaf Area Index (LAI) ([12], [13]). It is related to many physical processes such as radiation, energy, or mass exchanges. This parameter can be successfully predicted from NDVI, as shown by [8] for wheat canopies in Arizona. The dependence between NDVI and LAI can be approximated by a linear relationship for LAI values lower than 3. For LAI values greater than 3, the dependence of LAI on NDVI is no longer significant.

Thus, estimating IPAR or LAI from NDVI may not only be influenced by the nonlinear dependence of NDVI upon reflectance, but also by the nonlinearity of the relationship between NDVI and IPAR or LAI. Consider a landscape of surface st, composed of n elements. Each element 'i' of this landscape is characterized by its reflectance R_i, its vegetation index NDVI_i, its leaf area index LAI_i, its intercepted photosynthetically active radiation IPAR_i, and its surface s_i. The total reflectance R_t of the surface s_t is:

$$R_t = \sum_{i=1}^{n} R_i . s_i / s_t \tag{3}$$

so that

$$\mathrm{VIS}_t = \sum_{i=1}^{n} \mathrm{VIS}_i \cdot s_i / s_t$$

$$\mathrm{NIR}_t = \sum_{i=1}^{n} \mathrm{NIR}_i \cdot s_i / s_t \tag{4}$$

and the average NDVI over s_t is:

$$\mathrm{NDVI}_t = (\mathrm{NIR}_t - \mathrm{VIS}_t)/(\mathrm{NIR}_t + \mathrm{VIS}_t). \tag{5}$$

For this landscape, the actual LAI_t and IPAR_t are defined as follows:

$$\mathrm{LAI}_t = \sum_{i=1}^{n} \mathrm{LAI}_i \cdot s_i / s_t \tag{6}$$

$$\mathrm{IPAR}_t = \sum_{i=1}^{n} \mathrm{IPAR}_i \cdot s_i / s_t. \tag{7}$$

If we assume a linear relationship between NDVI and IPAR or LAI, (3) and (4) can be written:

$$\mathrm{LAI}_t = \alpha \sum_{i=1}^{n} \mathrm{NDVI}_i \cdot s_i / s_t + \beta \tag{8}$$

$$\mathrm{IPAR}_t = \alpha' \sum_{i=1}^{n} \mathrm{NDVI}_i \cdot s_i / s_t + \beta' \tag{9}$$

where α, β, α', and β' are constants determined at the local scale. We see from (5) and (6) that average radiometric measurements over s_t could be used to estimate LAI_t and IPAR_t only if NDVI_t, the average NDVI over s_t, can be expressed as:

$$\mathrm{NDVI}_t = \sum_{i=1}^{n} \mathrm{NDVI}_i \cdot s_i / s_t. \tag{10}$$

To illustrate the implications of this assumption, a theoretically simple case is considered: a site where all pixels are either composed of bare soil or dense canopy. All bare soil pixels have the same visible and near-infrared reflectances: $VIS = 0.165$ and $NIR = 0.188$; and for dense canopy pixels: $VIS = 0.22$ and $NIR = 0.61$ (these values correspond to typical *in situ* measurements at Ouango-Fitini (Ivory Coast). Fig. 1 compares the resulting NDVI_t with $\sum_{i=1}^{n} \cdot \mathrm{NDVI}_i \cdot s_i / s_t$ when the fractional canopy cover varies from 0 to 1. In general,

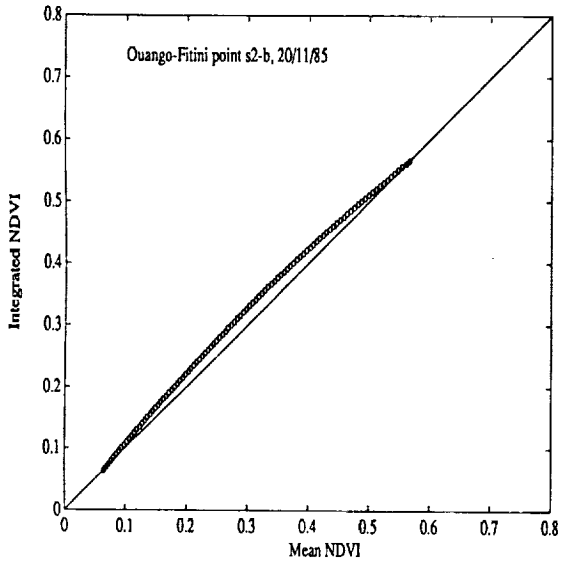

Fig. 1. Comparison between I_{NDVI} and M_{NDVI} when fractional vegetation cover varies from 0 to 1. Soil and vegetation radiances over Ouango-Fitini are used in the calculations.

$NDVI_t$ is smaller than $\sum_{i=1}^{n} NDVI_i \cdot s_i/s_t$. . The largest difference, 0.02 or 7%, is obtained for $NDVI_t$ values around 0.3. This difference is not negligible; it would introduce similar relative errors on $IPAR_t$ (α' is close to 1), but larger errors on LAI_t (α is typically equal to 2). In the limits (fractional canopy cover equal to 0 or 1), as expected there is no difference between $NDVI_t$ and $\sum_{i=1}^{n} NDVI_i \cdot s_i/s_t$.

As mentioned above, the relationships of NDVI versus IPAR or LAI are curvilinear for plant canopies (bare soils) at high (low) IPAR or LAI values. Investigating the contribution of each surface element to the integrated value of NDVI, therefore, requires a knowledge of the spatial distribution of vegetation. The problem is fairly complex, especially when the vegetation cover is heterogeneous.

III. Material

A. Study Areas

Three study areas, characterized by varied vegetation types, have been selected. The first two areas are located in West Africa, along a 550-km transect, covered by TM and HRV radiometer (Fig. 2(a)). This transect exhibits a large range of vegetation types (from woodland to shrub and grass steppe) and climatic conditions: the annual rainfall amount varies from 480 mm at Bidi (Burkina Faso) to 1280 mm at Ouango-Fitini (Ivory Coast). The annual rainfall distribution is unimodal and the vegetation of this zone is organized according to the rainfall gradient. The third area corresponds to a temperate agricultural site located in Beauce (France). This site is dominated by winter crops, but forests and urban zones are also present. The study areas are described in more details below.

1) Ouango-Fitini (Ivory Coast, 9°36'N–4°01'W): This site is located in the northern limit of the Comoe National Park. The climate is tropical with a dry season from November to April and a rainy season from May to October. The main vegetation types are [14]: dense-tree savanna and woodland, scattered tree savanna, and lowland and slope grass savanna, which represents 50, 30, and 10% of the total surface, respectively. The vegetation cover presents many large homogeneous zones and its seasonal evolution is related to alternating dry and rainy seasons.

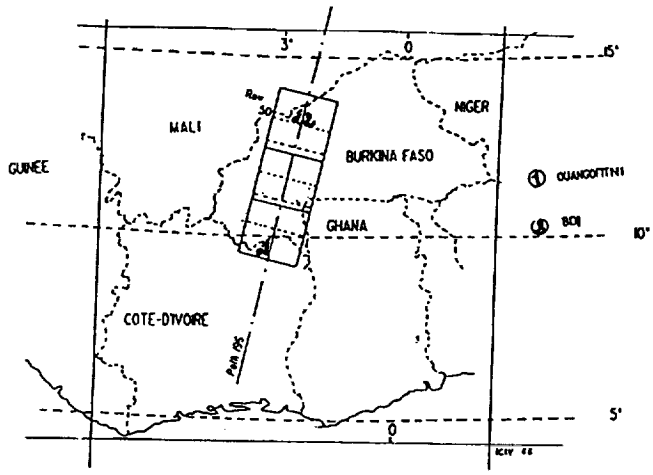

(a)

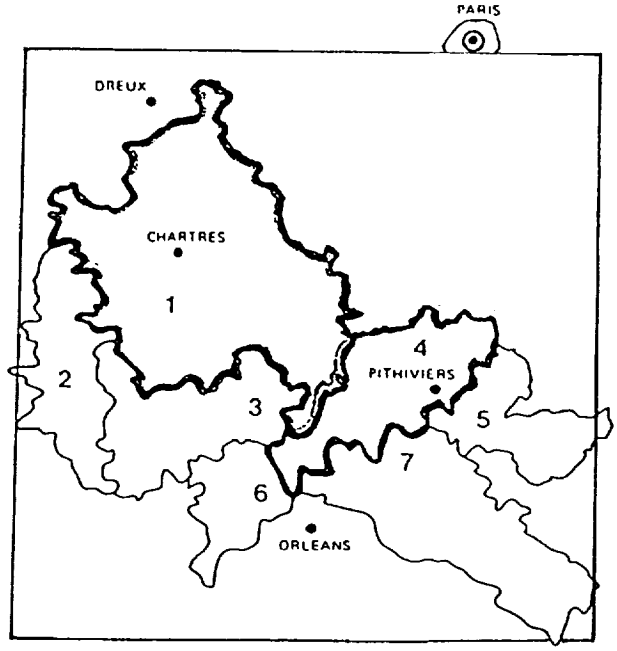

(b)

Fig. 2. Location of the test areas in West Africa (a) and in Beauce, France (b) (Kong *et al.* (1988).

2) Bidi (Burkina Faso, 13°55'N–2°30'W): This second site of tropical vegetation is located northwest of Burkina Faso, in the Yatenga Province. The rainy season is extremely short; it starts in July and ends in September. The main feature of the Bidi landscape is the scarcity of the vegetation cover except in the lowlands, where the tree cover (20–30%) includes tall trees and the grass cover reaches 90% at the end of the rainy season, but disappears during the dry season.

TABLE I
CHARACTERISTICS OF THE DATA USED IN THIS STUDY

Dates of Data Acquisition		
Name	Sensor	Dates
Ouango-Fitini		
wa	LANDSAT/TM	November 9, 1986
wb, w2	-"-	December 27, 1986
wc, w3	-"-	March 1, 1987
wd, w4	-"-	May 4, 1987
Bidi		
ba, b1	LANDSAT/TM	March 1, 1987
be, b4	-"-	May 4, 1987
bb, bc, bd	SPOT-1/HRV	October 4, 1987
Beauce		
ca, cb	SPOT-1/HRV	May 1986
cc, cd	-"-	June 1986
ce, cf, cg	-"-	October 1986
Visible and Near-Infrared Wavebands of the Two Sensor Systems		
Satellite System	Band Number	Waveband (nm)
LANDSAT/TM	3	630-690
	4	760-900
SPOT-1/HRV	2	610-680
	3	790-890

3) Beauce (France, 48°25'N–1°30'W): The region is mainly agricultural. The main crops are wheat, barley, corn, and green peas, and they represent 45, 10, 8, and 7% of the total surface, respectively. The period of interest is May–June 1986, which corresponds to the winter crop maturity (Fig. 2(b)).

B. Satellite Data

Multitemporal LANDSAT/TM and SPOT/HRV radiometer digital images are the primary sources of data used in this study. Information from the visible and near-infrared channels of the two sensor systems are used to compute NDVI. The spatial resolutions of the TM and HRV radiometer are 30 m and 20 m, respectively. Two subareas of 480×512 pixels are selected from Ouango-Fitini and Bidi at each date. Five subareas of the same size are selected from Beauce sites. For a given site, each subarea is representative of a type of landscape. Table I gives date and location of the images.

IV. METHODS

As the goal of the study is to investigate the spatial integration of NDVI, the original images are degraded to simulate spatial resolutions of 300 to 1000 m. Although there are differences in band center wavelength and width between current orbital instruments, there is no significant differences between the NDVI derived from visible and near-infrared channels of sensors such as TM and HRV radiometer [15].

High spatial resolution data are often used for simulation purposes and are an excellent tool in preparing future space missions [4]. For test sites, such as ours, a 20–30-m spatial resolution allows one to observe homogeneous objects [16]. Different methods are used to coarsen the spatial resolution from high spatial resolution data. A method based on averaging reduces the noise by smoothing the frequency distribution [4]. It also reduces the occurence of both high and low values. To avoid underestimation of the predicted values, methods based on the modulation transfer function (MTF) between initial and desired data are often used [4]. We shall assume that at a spatial resolution coarser than 300 m, the MTF is a rectangular window, so that the MTF characterizing the original images has no effect in the following study.

In our case, since the spatial degradation from original to coarser data is important (factor of 10 in resolution), we spatially average the data. From the original visible and near-infrared images of spatial resolution p, we generate a spatially degraded NDVI image of resolution $H = h \times p$ by aggregating h pixels in columns and p pixels in lines. The value of h is choosen to be a common multiple of the original resolutions of TM and HRV radiometer.

If x_{ij} and y_{ij} denote the visible and the near-infrared reflectances of a pixel (i, j), respectively, we define:

$$\overline{y} = 1/n \sum_{i=1}^{h} \sum_{j=1}^{h} y_{ij} \tag{11}$$

and

$$\overline{x} = 1/n \sum_{i=1}^{h} \sum_{j=1}^{h} x_{ij} \tag{12}$$

where $n = h^2$. The mean NDVI is then

$$\mathrm{M_{NDVI}} = (\overline{y} - \overline{x})/(\overline{y} + \overline{x}) \tag{13}$$

and represents the NDVI measured at the resolution $H = h \times p$.

The integrated value of NDVI at the resolution H, $\mathrm{I_{NDVI}}$, is defined as follows:

$$\mathrm{I_{NDVI}} = 1/n \sum_{i=1}^{h} \sum_{j=1}^{h} z_{ij} \tag{14}$$

with

$$z_{ij} = (y_{ij} - x_{ij})/(y_{ij} + x_{ij}). \tag{15}$$

On each spatially degraded image, a method of linear regression is applied to determine the relationship between $\mathrm{M_{NDVI}}$ and $\mathrm{I_{NDVI}}$. The coefficients of the linear regression are determined by least square minimization. The regression equation of $\mathrm{M_{NDVI}}$ versus $\mathrm{I_{NDVI}}$ is:

$$\mathrm{M_{NDVI}} = \alpha\, \mathrm{I_{NDVI}} + \beta \tag{16}$$

where β and α are the intercept and slope obtained by linear regression, respectively. These two coefficients are given by:

$$\alpha = r\, \sigma_{\mathrm{M_{NDVI}}}/\sigma_{\mathrm{I_{NDVI}}} \tag{17}$$

and

$$\beta = \overline{\mathrm{M}}_{\mathrm{NDVI}} - \alpha\, \overline{\mathrm{I}}_{\mathrm{NDVI}} \tag{18}$$

where r is the linear correlation coefficient between $\mathrm{I_{NDVI}}$ and $\mathrm{M_{NDVI}}$, and $\alpha_{\mathrm{M_{NDVI}}}$ and $\sigma_{\mathrm{I_{NDVI}}}$ are the standard deviations around the average values $\overline{\mathrm{M}}_{\mathrm{NDVI}}$ and $\overline{\mathrm{I}}_{\mathrm{NDVI}}$, respectively.

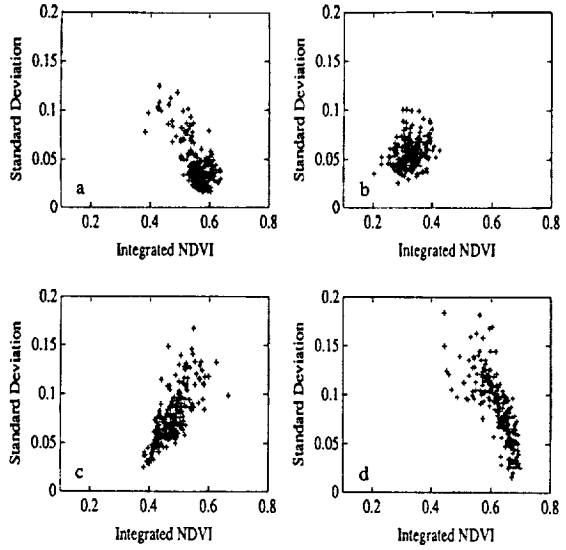

Fig. 3. Standard deviation $\sigma_{M_{NDVI}}$ versus M_{NDVI} over Ouango-Fitini on November 9, 1986 (a), Ouango-Fitini on March 1, 1987 (b), Bidi on October 4, 1987 (c), and Beauce in June 1986 (d).

V. Results And Discussion

A. Qualitative Description of M_{NDVI} Variability

The radiance measured by a coarse spatial resolution sensor such as AVHRR originates from different vegetation communities and soils whose characteristic sizes are generally lower than the resolution cell. In order to investigate the significance of M_{NDVI} provided by AVHRR, and understand the distribution of the objects inside each pixel, we have plotted the mean value of M_{NDVI} in 1-km areas as a function of corresponding $\sigma_{M_{NDVI}}$. Figs. 3(a), (b), (c), and (d) show the relationship between $\sigma_{M_{NDVI}}$ and M_{NDVI}.

At Ouango-Fitini, in November (biomass maximum), the values of M_{NDVI} at 1 km resolution are relatively high (between 0.5 and 0.6) and the values of $\sigma_{M_{NDVI}}$ are low (less than 0.06). In March (end of the dry season), the decrease in M_{NDVI} corresponds to the predominance of bare soil [17]. The highest values of M_{NDVI} are reached over islets of forest. The $\sigma_{M_{NDVI}}$ versus M_{NDVI} values are plotted on Figs. 3(a) and (b) for March and November, respectively.

At Bidi, in May (dry season), the values of M_{NDVI} and $\sigma_{M_{NDVI}}$ are low, between 0.15 and 0.2 and less than 0.04, respectively, and are explained by the smallness of the vegetation cover and the brightness of the soil. In October (end of the rainy season), the highest values of MNDVI are associated with the highest values of $\sigma_{M_{NDVI}}$ (Fig. 3(c)). A correlation coefficient of about 0.7 between M_{NDVI} and $\sigma_{M_{NDVI}}$ is computed, which is typical of heterogeneous vegetation. The highest values of M_{NDVI} are in agreement with [18]. In contrast to Ouango-Fitini, at the end of the rainy season, the vegetation is not uniform.

In Beauce, the behavior is different. In June, there is a global decrease of $\sigma_{M_{NDVI}}$ as function of M_{NDVI} (Fig. 3(d)). The highest M_{NDVI}'s correspond to low $\sigma_{M_{NDVI}}$'s because they are associated with homogeneous fields. Here, the correlation coefficient between M_{NDVI} and $\sigma_{M_{NDVI}}$ is about 0.8.

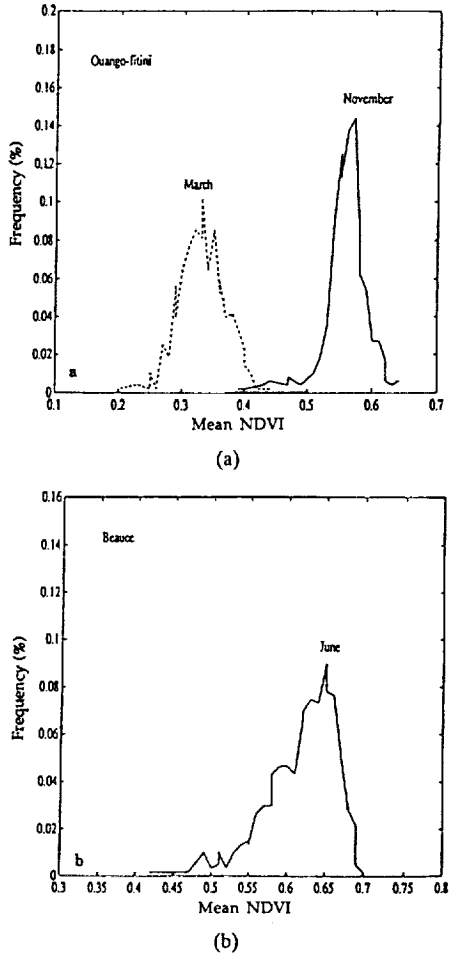

Fig. 4. Histogram of M_{NDVI} for Ouango-Fitini on November 9, 1986 and March 1,1987 (a) and for Beauce in June 1986 (b).

Three kinds of behavior can be noticed in Figs. 4(a) and (b), which show the frequency distribution of M_{NDVI}: (i) at Ouango-Fitini the landscape is largely dominated by a homogeneous vegetation cover at the end of the rainy season (Fig. 4(a)); (ii) at Bidi, there is a considerable influence of the bare soil, so that the landscape remains heterogeneous even at the end of the rainy season (Fig. 4(a)); (iii) in Beauce, the associated histogram exhibits a left dissymmetry in June associated with the predominance of mature crops (Fig. 4(b)).

B. Variability of M_{NDVI} with Regard to Spatial Resolution

Figs. 5(a), (b), and (c) show the relationship between heterogeneity and spatial resolution at various dates. M_{NDVI} is calculated (using the method described in section 4) at 300, 480, 600, and 960-m spatial resolutions. For each resolution, $\sigma_{M_{NDVI}}$ is calculated and plotted against resolution. The standard deviations corresponding to the original spatial resolution, i.e., 20 or 30 m, are also reported on the figures.

For Ouango-Fitini, at the end of the rainy season (November, Fig. 5(a)), the graph is flat and the $\sigma_{M_{NDVI}}$ is low (less than 0.25), showing that variability depends weakly on spatial resolution. In December (Fig. 4(a)), the graph exhibits a small peak at approximately 480 m. This behavior could be related to the regrowth of the leaves on the islets of forest [18] and could

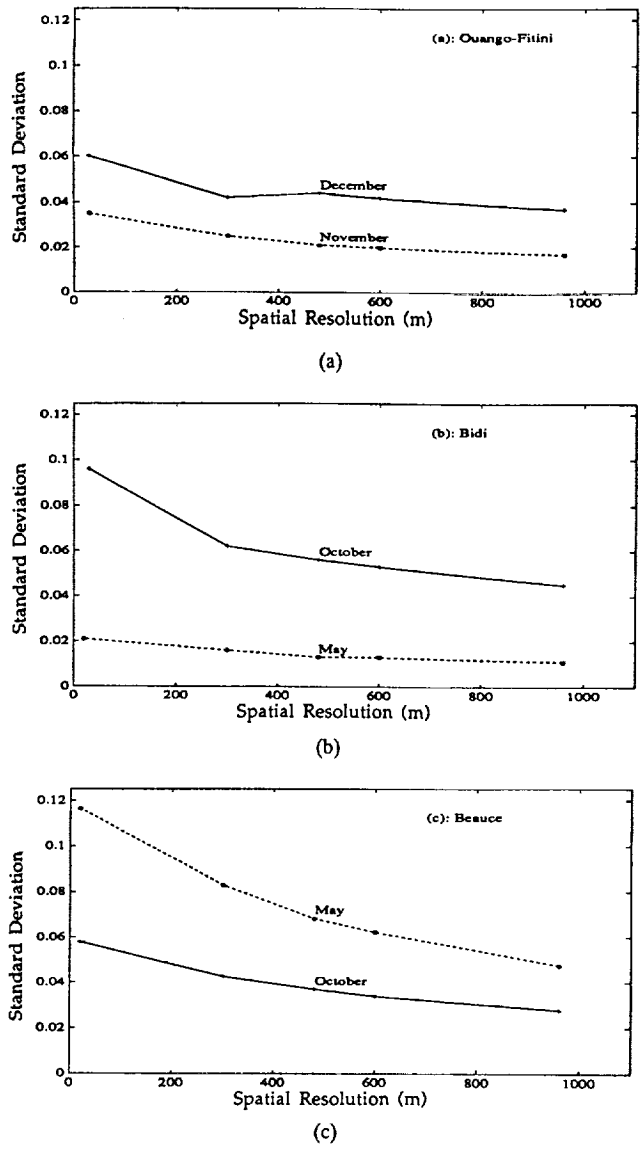

Fig. 5. Standard deviation $\sigma_{M_{NDVI}}$ versus spatial resolution over (a) Ouango-Fitini, (b) Bidi, and (c) Beauce.

be a manifestation of the dephasing cycle between herbaceous and ligneous stratas.

For Bidi, in May (Fig. 5(b)), the graph is flat and the $\sigma_{M_{NDVI}}$ is low (in general less than 0.02). Since the vegetation is dry, the adjacent values of NDVI are strongly correlated, which induces little or no spatial variation from one pixel to another at coarse resolutions. At the end of the rainy season (October, Fig. 5(b)), the graph exhibits a high value at the initial resolution and remains flat between 300 and 480 m. It is difficult to relate this scale to a specific type of vegetation cover [19], but small patches of vegetation may be present in the landscape at this date.

For Beauce, in May (Fig. 5(c)), the large decrease in $\sigma_{M_{NDVI}}$ between 30 and 300 m is due to the diversity of this agricultural region and to the mixing of active crops and bare soils or to poorly covered plots. In October, bare soils and harvested crops are predominant, and the decrease in variability between 30 and 300 m is small.

The main conclusion is that the loss of spatial variability is larger between the original resolution of 20 or 30 m and 300 m than between 300 and 1000 m, and that the variability is not significantly affected by spatial resolution in the range 300–1000 m.

C. Spatial Integration of NDVI

It has been shown in [20] that a linear relationship exists between AVHRR reflectances and Multi-Spectral Scanner (MSS) reflectances degraded to 1 km resolution. The problem is different for NDVI, because the equality between M_{NDVI} and I_{NDVI} is algebrically false. In this section we quantify the relationship between M_{NDVI} and I_{NDVI} and study the influence of spatial variability on the relationship.

1) Relationship Between M_{NDVI} and I_{NDVI}: The linear correlation coefficient r between M_{NDVI} and I_{NDVI} at 1-km resolution (Figs. 6(a), (b), (c) and Table II) is high (above 0.99). Comparable results are observed for other spatial resolutions, namely, 300, 480, and 600 m for Ouango-Fitini, Bidi, and Beauce test sites, whatever the date of acquisition (see Table III for 300-m resolution). Thus, the high linear correlation between the two indices does not depend on time, spatial resolution, and land cover type.

The slope α, on the contrary, varies with time, spatial resolution, and land cover type; but globally, it remains close to 1. Its variation with spatial resolution, weaker at Ouango-Fitini than at Bidi, will be analyzed below.

The intercept β does not exhibit coherent variations. Its maximum value is lower than 0.02 over all test sites (Tables II and III). Furthermore the values remain close to zero at all simulated spatial resolutions. Globally, positive values correspond to low α values ($\beta > 0$ when $\alpha < 1$).

2) Influence of the Spatial Variability on α: As reported, the correlation coefficient r between I_{NDVI} and M_{NDVI} and the intercept β do not present significant variations for all the scenes considered. The slope α is the only parameter whose variations with spatial variability needs to be studied. For a given spatial resolution H, a linear relationship exists between $\sigma_{M_{NDVI}}$ and $\sigma_{I_{NDVI}}$ with a very significant correlation coefficient of 0.999. This relationship can be written:

$$\sigma_{M_{NDVI}} = a(H)\,\sigma_{I_{NDVI}} + b(H). \tag{19}$$

Combining (11a) and (12) yields:

$$\alpha(H,t) = r[a(H) + b(H)/\sigma_{I_{NDVI}}(H,t)] \tag{20}$$

where t represents time ($\sigma_{I_{NDVI}}$ may vary with time for a given test site).

On the one hand, (13) indicates that if H is kept constant, then α will depend only on $\sigma_{I_{NDVI}}$. Eq. (13) predicts that α increases when $\sigma_{I_{NDVI}}$ decreases, and conversely. This agrees with the observed variability of I_{NDVI} (Section IV). Moreover, the results are valid for all spatial resolutions considered (see Tables II and III for 1000 and 300-m resolutions).

On the other hand, the variations of $\sigma_{I_{NDVI}}$ and α with respect to H when t is fixed are weaker (Figs. 5(a), (b), and (c)). When the spatial resolution coarsens from 300 m to 1 km, the coefficient $a(H)$ decreases globally from 1.004 to 0.973 at Ouango-Fitini, and from 0.980 to 0.946 at Bidi, while it

TABLE II
MEAN OF I_{NDVI} (E(Ind)), ITS STANDARD DEVIATION (σ_{IND}), MEAN OF M_{NDVI}(E(Mnd)), ITS STANDARD DEVIATION (σ_{Mnd}), ROOT MEAN SQUARE ERROR (RMSE) BETWEEN I_{NDVI} AND M_{NDVI}, CORRELATION COEFFICIENT (r), SLOPE (α), AND INTERCEPT (β) AT 1-KM RESOLUTION FOR ALL TEST SITES AND DATES

Resolution: 1 km								
Sites	E(Ind)	σ_{Ind}	E(Mnd)	σ_{Mnd}	RMSE	r	α	β
Ouango-Fitini								
w2	0.376	0.040	0.379	0.040	0.00328	0.998	1.009	-0.00101
w3	0.324	0.037	0.327	0.036	0.00378	0.998	0.983	0.00817
w4	0.595	0.055	0.596	0.055	0.00179	1.000	1.008	-.00366
wa	0.559	0.017	0.560	0.017	0.00086	0.999	1.014	-0.00749
wb	0.372	0.037	0.374	0.036	0.00244	0.999	0.993	0.00439
wc	0.337	0.034	0.339	0.033	0.00284	0.998	0.995	0.00335
wd	0.569	0.036	0.569	0.035	0.00092	1.000	1.009	-0.00480
Bidi								
b1	0.205	0.029	0.201	0.026	0.00552	0.996	0.904	0.01554
b4	0.179	0.009	0.178	0.009	0.00067	0.999	0.969	0.00501
ba	0.201	0.034	0.197	0.030	0.00587	0.997	0.903	0.01528
bb	0.482	0.045	0.478	0.042	0.00557	0.997	0.950	0.01940
bc	0.511	0.048	0.506	0.046	0.00639	0.999	0.956	0.01679
bd	0.527	0.034	0.521	0.033	0.00599	0.998	0.976	0.00716
be	0.176	0.011	0.176	0.010	0.00066	0.999	0.976	0.00383
Beauce								
ca	0.350	0.048	0.351	0.048	0.00334	0.998	1.023	-0.00721
cb	0.305	0.051	0.304	0.052	0.00218	0.999	1.015	-0.00539
cc	0.622	0.036	0.623	0.036	0.00404	0.994	0.997	0.00308
cd	0.579	0.051	0.579	0.052	0.00296	0.998	1.010	-0.00536
ce	0.001	0.028	0.008	0.025	0.00762	0.994	0.916	0.00676
cf	0.010	0.017	0.015	0.016	0.00490	0.995	0.904	0.00531
cg	0.026	0.017	0.030	0.016	0.00469	0.995	0.904	0.00661

increases from 1.04 to 1.08 in the Beauce region. Examining Figs. 5(a), (b), and (c) in detail, more complex variations corresponding to those of the slope α can be observed. The fluctuations of $b(H)$ are more irregular and do not present any significant trend. In general, absolute values of b(H) remain lower than 10^{-3}, except for Beauce, and $b(H)/\sigma_{I_{NDVI}}$ is about 10^{-2}. The variations of both $a(H)$ and $b(H)/\sigma_{I_{NDVI}}$ are of about 10^{-2}, for all land cover types and states. In summary, these variations are weaker than the variations of α and $\sigma_{I_{NDVI}}$ with respect to time.

3) α Simulation: In order to further test the significance of the slope α simulated using (13), this slope is compared with that obtained from the linear regression between M^{NDVI} and I_{NDVI} (Tables IV and V). Simulated and observed values of α are also plotted versus time on Figs. 7(a), (b), and (c).

On average, there is no significant difference between observed and simulated slopes, except for Bidi and Beauce in November 1986 and October 1986, respectively, where it exceeds 0.045. Elsewhere, the maximum errors between simulated and observed α values are lower than 0.025 for all the studied test sites (Tables IV and V).

C. Accuracy of the Spatial Integration

When computing M_{NDVI}, the contribution of each vegetation species is not weighted by the fraction of the surface it covers. The resulting error can be estimated by the root mean square difference (RMSE) between the M_{NDVI} and I_{NDVI}:

$$\mathrm{RMSE} = \left[1/n \sum_{i=1}^{n} (M_{NDVI} - I_{NDVI})^2\right]^{1/2} \tag{21}$$

where n corresponds to the number of pixels at the resolution considered.

This RMSE was calculated at the different dates, spatial resolutions, and test sites studied in this paper (see Tables II and III). The results indicate that the maximum error introduced when assimilating I_{NDVI} to M_{NDVI} is less than $6.4\ 10^{-3}$.

In order to interpret the RMSE values obtained, a limited development analysis is carried out. Each NIR and VIS is expressed as:

$$\begin{aligned} NIR_i &= \overline{NIR} + nir_i \\ VIS_i &= \overline{VIS} + vis_i \end{aligned} \tag{22}$$

where $\overline{NIR}$ and $\overline{VIS}$ are the mean values for a given spatial resolution. Using these expressions to relate I_{NDVI} to M_{NDVI}

TABLE III
MEAN OF I_{NDVI}(E(Ind)), ITS STANDARD DEVIATION (σ_{Ind}), MEAN OF M_{NDVI}(E(Mnd)), ITS STANDARD DEVIATION (σ_{Mnd}), ROOT MEAN SQUARE ERROR (RMSE) BETWEEN I_{NDVI} AND M_{NDVI}, CORRELATION COEFFICIENT (r), SLOPE (α), AND INTERCEPT (β) AT 300-M RESOLUTION FOR ALL TEST SITES AND DATES

Resolution: 300 m								
Sites	E(Ind)	σ_{Ind}	E_{Mnd}	σ_{Mnd}	RMSE	r	α	β
Ouango-Fitini								
w2	0.391	0.047	0.392	0.047	0.00197	0.999	1.000	0.00116
w3	0.319	0.052	0.321	0.052	0.00260	0.999	0.997	0.00278
w4	0.575	0.062	0.575	0.062	0.00151	1.000	1.006	-0.00271
wa	0.562	0.024	0.562	0.024	0.00077	1.000	1.006	-0.00311
wb	0.387	0.041	0.388	0.041	0.00162	1.000	0.995	0.00279
wc	0.327	0.041	0.328	0.041	0.00263	0.998	0.997	0.00210
wd	0.574	0.045	0.574	0.045	0.00118	1.000	1.007	-0.00351
Bidi								
b1	0.203	0.035	0.200	0.033	0.00444	0.998	0.938	0.00948
b4	0.178	0.011	0.178	0.011	0.00057	1.000	0.981	0.00301
ba	0.207	0.051	0.203	0.048	0.00576	0.998	0.940	0.00884
bb	0.483	0.061	0.480	0.059	0.00483	0.999	0.967	0.01218
bc	0.511	0.067	0.507	0.065	0.00500	0.999	0.979	0.00679
bd	0.527	0.053	0.522	0.052	0.00512	0.999	0.981	0.00540
be	0.177	0.015	0.177	0.015	0.00061	1.000	0.982	0.00276
Beauce								
ca	0.350	0.082	0.350	0.084	0.00386	0.999	1.013	-0.00427
cb	0.305	0.082	0.304	0.082	0.00260	1.000	1.006	-0.00234
cc	0.621	0.072	0.622	0.072	0.00455	0.998	1.002	-0.00031
cd	0.578	0.074	0.579	0.074	0.00292	0.999	1.005	-0.00274
ce	0.000	0.042	0.004	0.041	0.00525	0.997	0.961	0.00387
cf	0.010	0.030	0.012	0.029	0.00375	0.997	0.958	0.00304
cg	0.025	0.030	0.028	0.029	0.00338	0.997	0.963	0.00316

leads to (23) at bottom of page. Limiting the development of the previous equation to the second order in reflectance yields:

$$I_{NDVI} = M_{NDVI}(1 + A + B + \varepsilon) \tag{24}$$

where

$$A = (\mathrm{Var(NIR)} - \mathrm{Var(VIS)})/\left(\overline{\mathrm{NIR}^2} - \overline{\mathrm{VIS}^2}\right)$$
$$B = [\mathrm{Var(NIR)} + \mathrm{Var(VIS)} + 2\,\mathrm{Cov(NIR, VIS)}]/\left(\overline{\mathrm{NIR}} + \overline{\mathrm{VIS}}\right)^2 \tag{25}$$

and ϵ is the residu. The variance and covariance functions, Var and Cov, are given by:

$$\mathrm{Var(NIR)} = 1/n \sum_{i=1}^{n} \mathrm{nir}_i^2$$
$$\mathrm{Var(VIS)} = 1/n \sum_{i=1}^{n} \mathrm{vis}_i^2$$
$$\mathrm{Cov(NIR, VIS)} = 1/n \sum_{i=1}^{n} \mathrm{nir}_i \cdot \mathrm{vis}_i. \tag{26}$$

The terms A and B in (14) depend in a complicated way on the mean, variance, and covariance of the visible and near-infrared reflectances characterizing the pixels within the coarse

$$I_{NDVI} = 1/n \sum_{i=1}^{n} \left[\overline{\mathrm{NIR}} - \overline{\mathrm{VIS}} + \mathrm{nir}_i - \mathrm{vis}_i\right]/\left[\overline{\mathrm{NIR}} + \overline{\mathrm{VIS}} + \mathrm{nir}_i + \mathrm{vis}_i\right]$$

$$I_{NDVI} = M_{NDVI}\ 1/n \sum_{i=1}^{n} \left[1 + (\mathrm{nir}_i - \mathrm{vis}_i)/\left(\overline{\mathrm{NIR}} - \overline{\mathrm{VIS}}\right)\right]/\left[1 + (\mathrm{nir}_i + \mathrm{vis}_i)/\left(\overline{\mathrm{NIR}} + \overline{\mathrm{VIS}}\right)\right]. \tag{23}$$

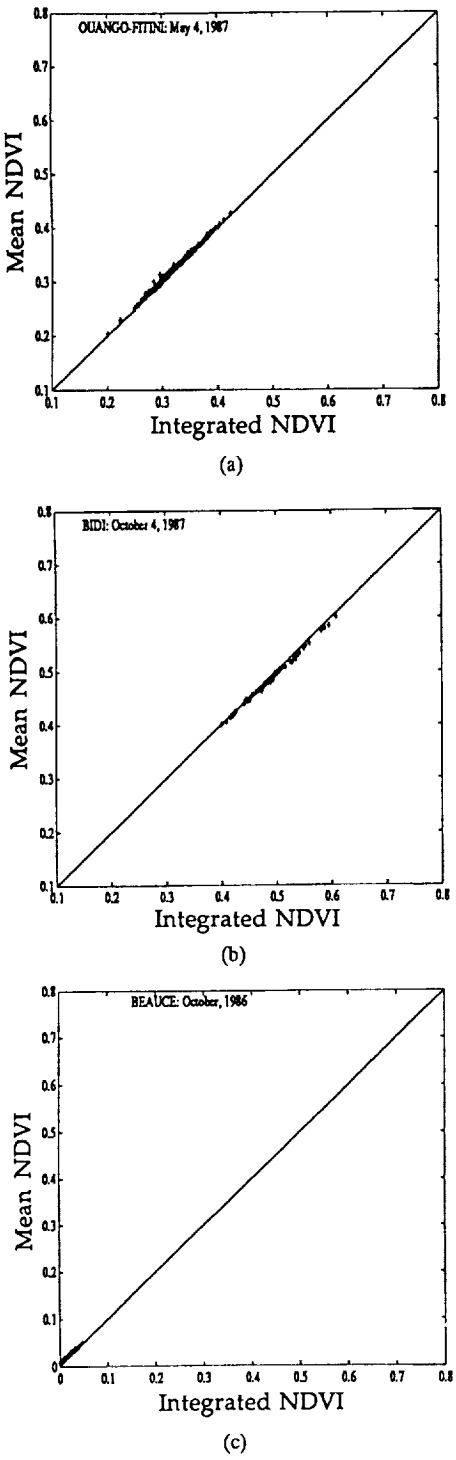

Fig. 6. Mean NDVI (M_{NDVI}) versus Integrated NDVI (I_{NDVI}) on May 4, 1987 at Ouango-Fitini (a), on October 4, 1987 at Bidi (b), and on October 4, 1987 in Beauce (c).

spatial resolution areas. Since $\overline{NIR}$ is generally greater than $\overline{VIS}$, the sign of A is essentially linked to the difference between Var(NIR) and Var(VIS). The term B can also be positive or negative depending on the sign and relative importance of Cov(NIR, VIS). *A priori*, there is no reason for the various parameters to combine such that $A + B = 0$. The natural variability of the land cover and the reflectance values encountered in the real world, however, may minimize $A + B$.

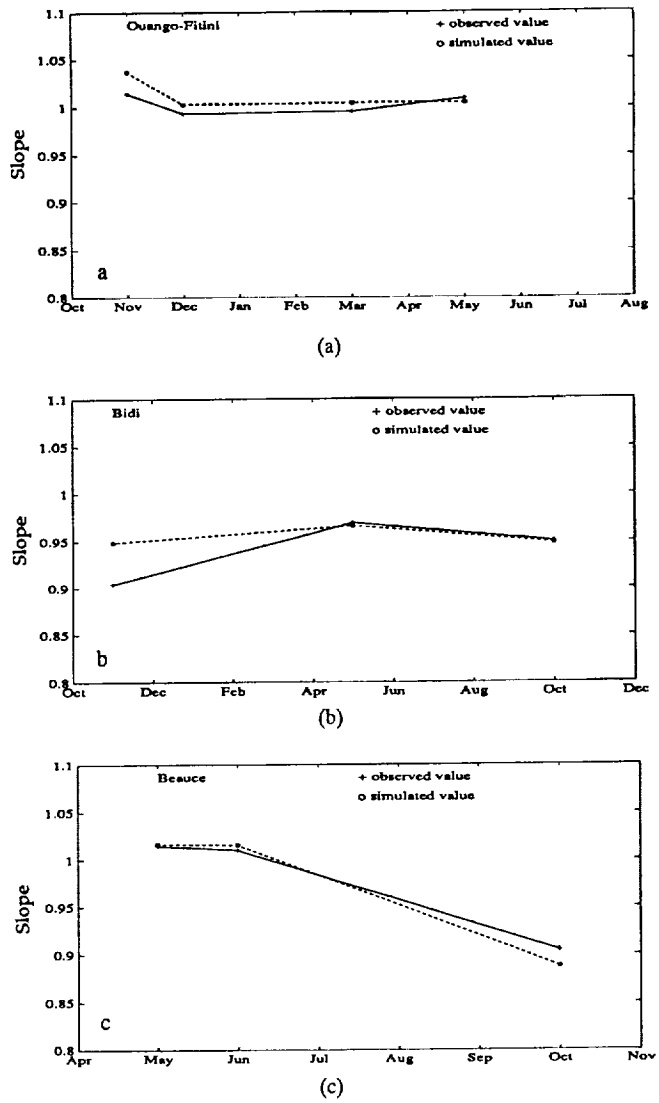

Fig. 7. Time evolution of simulated and observed values of the slope α for Ouango-Fitini (a), Bidi (b), and Beauce (c).

Let us now examine (24) using actual data. For the three sites and all dates, the absolute value of ϵ remains small, typically 5 10^{-4} (see Table VI). Therefore, (24) may be justifiably written:

$$I_{NDVI} = M_{NDVI}(1 + A + B). \tag{27}$$

The mean absolute values of M_{NDVI} $(A + B)$ are small (less than 6.15 10^{-3}) for all sites and dates, which confirms the results displayed in Figs. 6(a), (b), and (c) and Tables II and III. The small difference between I_{NDVI} and M_{NDVI} may be explained by the values of the parameters in the expressions of A and B (see Tables VI and VII). In general, Var(VIS), Var(NIR), and Cov(NIR,VIS) are much less than $\overline{NIR^2} - \overline{VIS^2}$ and, *a fortiori*, $(\overline{NIR} + \overline{VIS})^2$. The maximum value of M_{NDVI} $(A + B)$, however, is 6.9 10^{-2} in the case of Bidi and Ouango-Fitini and 1.7 in the case of Beauce. This is due to pixels containing bare soil and vegetation (Ouango-Fitini) or bare soil (Beauce in October). When there is no vegetation, the difference $\overline{NIR^2} - \overline{VIS^2}$ (i.e., the denominator in the expression of A) is small, yielding a high A value. The

TABLE IV
OBSERVED (α_{obs}) AND SIMULATED (α_{simu}) SLOPE, WITH THE CORRESPONDING CORRELATION COEFFICIENT (r), STANDARD-DEVIATION (σ_I), AND INTERCEPT (β) FOR ALL SITES AND DATES AT 1-KM SPATIAL RESOLUTION

Sites	α_{obs}	α_{simu}	r	σ_I	β
Ouango-Fitini:					
w2	1.009	1.000	0.998	0.0396	-0.00101
w3	0.983	1.001	0.997	0.0373	0.00817
w4	1.008	0.993	0.999	0.0548	-0.00366
wa	1.014	1.037	0.999	0.0172	-0.00749
wb	0.993	1.003	0.999	0.0369	0.00439
wc	0.995	1.004	0.997	0.0336	0.00335
wd	1.009	1.005	0.999	0.0355	-0.00480
Bidi:					
b1	0.90401	0.94853	0.995	0.0289	0.01554
b4	0.96922	0.96618	0.999	0.0093	0.00501
ba	0.90304	0.94871	0.996	0.0336	0.01528
bb	0.95041	0.94875	0.998	0.0451	0.01940
bc	0.95622	0.94874	0.998	0.0484	0.01679
bd	0.97575	0.95002	0.998	0.0344	0.00716
be	0.97557	0.96283	0.999	0.0112	0.00383
Beauce:					
ca	1.02273	1.01026	0.998	0.0475	-0.00721
cb	1.01487	1.01684	0.999	0.0514	-0.00539
cc	0.99699	0.98654	0.994	0.0367	0.00308
cd	1.01035	1.01590	0.998	0.0513	-0.00536
ce	0.91554	0.95744	0.993	0.0278	0.00676
cf	0.90443	0.88800	0.994	0.0174	0.00531
cg	0.90441	0.88760	0.995	0.0173	0.00661

TABLE V
OBSERVED (α_{obs}) AND SIMULATED (α_{simu}) SLOPE, WITH THE CORRESPONDING CORRELATION COEFFICIENT (r), STANDARD DEVIATION (σ_I), AND INTERCEPT (β) FOR ALL SITES AND DATES AT 300-M SPATIAL RESOLUTION

Sites	α_{obs}	α_{simu}	r	σ_I	β
Ouango-Fitini:					
w2	0.999	1.001	0.999	0.0476	0.00116
w3	0.996	1.001	0.999	0.0523	0.00278
w4	1.005	1.001	0.999	0.0620	-0.00271
wa	1.006	0.999	0.999	0.0245	-0.00311
wb	0.995	1.000	0.999	0.0416	0.00279
wc	0.996	0.999	0.998	0.0419	0.00210
wd	1.006	1.001	0.999	0.0454	-0.00351
Bidi:					
b1	0.938	0.963	0.997	0.0359	0.00948
b4	0.980	0.952	0.999	0.0115	0.00301
ba	0.940	0.965	0.997	0.0518	0.00884
bb	0.967	0.967	0.999	0.0619	0.01218
bc	0.978	0.967	0.999	0.0670	0.00679
bd	0.981	0.966	0.999	0.0536	0.00540
be	0.982	0.957	0.999	0.0157	0.00276
Beauce:					
ca	1.013	1.008	0.999	0.0828	-0.00427
cb	1.006	1.008	0.999	0.0820	-0.00234
cc	1.001	1.002	0.998	0.0723	-0.00031
cd	1.005	1.005	0.999	0.0741	-0.00274
ce	0.961	0.976	0.997	0.0425	0.00387
cf	0.957	0.951	0.996	0.0304	0.00304
cg	0.963	0.952	0.997	0.0308	0.00316

above cases, however, are isolated and cannot be considered as representative of the entire set of images.

When the spatial resolution is 1 km, the average RMSE value for all cases considered is 0.0036, which corresponds to less than 1% of the average integrated NDVI value over all test sites and dates (see Table II). For individual sites and dates, the figures are similar, except for Beauce in Oct. (RMSE value reaching 0.0076). The 1% value is much smaller than that expected theoretically. In Section II we have indicated that for Ouango-Fitini the difference between I_{NDVI} and M_{NDVI} should be about 6% when I_{NDVI} is around 0.3. A possible explanation is that distinction between bare soil and vegetation cannot be clearly made even at the local scale, or that the principal scales of variability are smaller than the size of the TM and HRV radiometer pixels.

It is necessary to compare the 0.0036 value to the errors linked, on one hand, to the NDVI itself, namely those resulting from corrections of atmospheric and surface directional effects, and, on the other hand, to the empirical relationships between NDVI and vegetation parameters such as IPAR and LAI. Atmospheric effects can induce errors of typically 0.02 and 0.06 on the absolute NDVI value due to atmospheric water vapor and aerosols [21], respectively. The complete correction of these perturbing effects, especially aerosol scattering, as well as surface directional effects is not possible. The empirical relationships between NDVI and vegetation parameters also exhibit significant errors. The accuracies of the associated physical parameterizations (e.g., [9], [22]) are often an order of magnitude greater than the RMSE values reported in this paper. For example, [9] found a RMSE of 0.053 in the linear relationship between NDVI and IPAR they established from field measurements. Thus the errors introduced when using M_{NDVI} instead of I_{NDVI} are one order of magnitude lower than the residual errors after radiometric corrections of NDVI and those induced by the physical parameterizations. We conclude that using NDVI derived from coarse spatial resolution sensor (e.g., NOAA/AVHRR) data in relationships determined at the local scale will not introduce significant errors in the estimated biophysical parameters, at least for the situations selected and until more accurate relationships between NDVI and biophysical parameters are established.

VI. CONCLUSION

This study, achieved on two West African tropical sites and one French temperate site, shows that, for a spatial resolution lower than 1000 m (300–1000 m), the integrated NDVI, I_{NDVI},

TABLE VI
MEAN VALUES OF VARIOUS TERMS OF THE SECOND-ORDER LIMITED DEVELOPMENT OF I_{NDVI} VERSUS M_{NDVI} AT 1-KM RESOLUTION (SEE (24))

Site	E(Pr*)	E(Var(VIS))	E(Var(NIR))	E(Cov)	E(VIS)	E(NIR)	$E(\epsilon)$
Ouango-Fitini:							
w2	-0.00234	0.00008	0.00056	0.00013	0.071	0.160	0.0000129
w3	-0.00257	0.00013	0.00072	0.00013	0.105	0.207	-0.0001526
w4	-0.00087	0.00007	0.00041	-0.00003	0.063	0.251	-0.0000079
wa	-0.00054	0.00003	0.00027	0.00001	0.075	0.268	-0.000012
wb	-0.00186	0.00008	0.00051	0.00011	0.082	0.181	-0.0000903
wc	-0.00147	0.00018	0.00075	0.00019	0.111	0.225	-0.0003377
wd	-0.00034	0.00005	0.00029	0.00001	0.066	0.243	-0.0000481
Bidi							
b1	0.00378	0.00165	0.00093	0.00098	0.258	0.388	0.0003063
b4	0.00049	0.00039	0.00043	0.00036	0.276	0.396	0.0000086
ba	0.00392	0.00175	0.00108	0.00106	0.260	0.387	0.0002967
bb	0.00439	0.00036	0.00021	0.00008	0.085	0.241	0.0000814
bc	0.00553	0.00043	0.00020	0.00009	0.083	0.254	-0.0000002
bd	0.00546	0.00041	0.00013	0.00007	0.080	0.254	0.0001004
be	0.00047	0.00041	0.00046	0.00038	0.282	0.402	0.0000070
Beauce							
ca	-0.00058	0.00022	0.00040	-0.00008	0.076	0.159	-0.0001627
cb	0.00103	0.00021	0.00024	-0.00006	0.084	0.158	-0.0001823
cc	-0.00076	0.00019	0.00054	-0.00012	0.049	0.214	-0.0004332
cd	-0.00052	0.00015	0.00046	-0.00007	0.057	0.215	-0.0001040
ce	-0.00615	0.00004	0.00013	0.00007	0.060	0.061	-0.0004636
cf	-0.00398	0.00003	0.00009	0.00005	0.061	0.063	-0.0002916
cg	-0.00392	0.00005	0.00012	0.00007	0.064	0.068	-0.0001610

TABLE VII
VALUES OF VARIOUS TERMS OF THE SECOND-ORDER LIMITED DEVELOPMENT OF I_{NDVI} VERSUS M_{NDVI} AT 1-KM RESOLUTION. THEY CORRESPOND TO THE PARCEL WHERE THE DIFFERENCE BETWEEN I_{NDVI} AND M_{NDVI} IS THE MOST SIGNIFICANT (SEE (24))

Site	Pr*	Var(VIS)	Var(NIR)	Cov	E(VIS)	E(NIR)	ϵ
Ouango-Fitini							
w2	-0.02978	0.00006	0.00102	0.00004	0.060	0.142	0.0015177
w3	-0.05810	0.00009	0.00215	0.00026	0.087	0.167	-0.0003752
w4	-0.01257	0.00012	0.00187	-0.00039	0.052	0.277	0.0004974
wa	-0.00716	0.00003	0.00192	0.00009	0.075	0.302	-0.0000599
wb	-0.01694	0.00006	0.00096	0.00004	0.074	0.179	-0.0002013
wc	-0.03796	0.00021	0.00219	0.00047	0.100	0.188	-0.0012388
wd	-0.00560	0.00002	0.00081	-0.00004	0.046	0.234	-0.0003404
Bidi							
b1	0.07546	0.00618	0.00221	0.00331	0.239	0.399	0.0013984
b4	0.00829	0.00072	0.00034	0.00047	0.281	0.411	0.0001481
ba	0.06870	0.00581	0.00179	0.00279	0.241	0.407	0.0015708
bb	0.02688	0.00115	0.00018	0.00011	0.084	0.270	0.0003420
bc	0.03234	0.00118	0.00052	0.00055	0.082	0.271	-0.0001524
bd	0.02198	0.00069	0.00027	0.00032	0.069	0.255	0.0008218
be	0.01153	0.00097	0.00065	0.00077	0.257	0.386	0.0000256
Beauce							
ca	-0.01882	0.00026	0.00118	-0.00036	0.073	0.193	-0.0000233
cb	-0.01430	0.00026	0.00080	-0.00025	0.079	0.173	0.0006012
cc	0.04867	0.00128	0.00181	0.00062	0.058	0.205	-0.0228064
cd	0.02356	0.00070	0.00020	0.00006	0.075	0.219	-0.0024748
ce	0.29578	0.00005	0.00019	0.00010	0.051	0.045	0.0020951
cf	0.52351	0.00004	0.00018	0.00008	0.061	0.059	0.0005623
cg	-1.72490	0.00020	0.00043	0.00028	0.063	0.064	0.0033479

*Pr=M_{NDVI} $(A + B)$

is linearly correlated to the spatial average of NDVI, M_{NDVI}. The slope of I_{NDVI} versus M_{NDVI} depends only on the structure state of the surface, which can be expressed by the spatial variability of the canopy cover, in terms of the standard deviation $\sigma_{I_{NDVI}}$.

In general, the slope and intercept of the linear regressions are close to 1 and 0, respectively, and, hence, the error induced when I_{NDVI} is used instead of M_{NDVI} is small (average RMSE of 0.0036). This error is often an order of magnitude lower than either the residual errors after radiometric corrections on NDVI or the errors induced by the current physical parametrizations. The small differences between I_{NDVI} and M_{NDVI} are shown to be directly linked to the small variance and covariance of the visible and near-infrared reflectances Var(VIS), Var(NIR), and Cov(NIR,VIS) when compared to the mean quantities $\overline{NIR^2} - \overline{VIS^2}$ and $\left(\overline{NIR} + \overline{VIS}\right)^2$. Theoretical considerations, however, suggest that much higher differences should be found. The discrepancy might originate from the fact that bare soil areas are not apparent, even at the local scale; but it is also possible that the spatial variability is concentrated at scales smaller than the size of the TM and HRV radiometer pixels.

Nevertheless, we conclude that NDVI, even though it is not a linear combination of radiances or reflectances, can be spatially integrated without significant loss of information. Further validations, however, need to be carried out for other land cover types than tropical savanna or temperate crop to assess whether using M_{NDVI} instead of I_{NDVI} is generally adequate.

The use of remotely sensed data to estimate biophysical parameters of vegetation dynamic models may solve a large part of the problems linked to spatial integration and scale change. The question, however, is to find inverse relationships between remotely sensed data and the biophysical parameters. The NDVI, thanks to its ability to be linearly integrated and to relate to major canopy parameters, appears as a useful radiometric index for the global parameterization of vegetation-related processes such as primary production and heat and mass transfer between the land surface and the atmosphere.

REFERENCES

[1] EOS Steering Committee Report, vol.II, 1989.
[2] IGBP Rep. no. 12, 1990.
[3] J.R.G. Townshend and C.O. Justice, "Selecting the spatial resolution of satellite sensors required for global monitoring of land transformations," *Int. J. Remote Sensing*, vol. 2, pp. 187–236, 1988.
[4] C.O. Justice, B.L. Markham, J.R.E. Townshend, and R.L. Kennard, "Spatial degradation of satellite data," *Int. J. Remote Sensing*, vol. 10, pp. 1539–1561, 1989.
[5] C. J. Tucker, "Red and photographic infrared linear combinations for monitoring vegetation," *Remote Sensing of Environment*, vol. 8, pp. 127–150, 1979.
[6] J. D. Tarpley, S. R. Schneider, and R. L. Money, "Global vegetation indices from the NOAA-7 Meteorological satellite," *J. Climate and Applied Meteorology*, vol. 23, pp. 491–493, 1984.
[7] P. J. Sellers, "Canopy reflectance, photosynthesis and transpiration," *Int. J. Remote Sensing*, vol. 6, pp. 1335–1372, 1985.
[8] G. Asrar, M. Fuchs, E.T. Kanemasu, and J. L. Hatfield, "Estimating absorbed photosynthetic radiation and leaf area index from spectral reflectance in wheat," *Agronomy J.*, vol. 76, pp. 300–306, 1984.
[9] J. L. Hatfield, G. Asrar, E. T. Kanemasu, "Intercepted photosynthetically active radiation estimated by spectral reflectances," *Remote Sensing of Environment*, vol. 14, pp. 65–67, 1984.
[10] G. Asrar, E. T. Kanemasu, G. P. Miller, and R. L. Weiser, "Light interception and leaf area estimates from measurements of grass canopy reflectances," *IEEE Trans. Geosci. Remote Sensing* vol. GE-24, no. 1, pp. 76–82, 1986.
[11] B. J. Choudhury, "Relationships between vegetation indices, radiation absorption, and net photosynthesis evaluated by a sensitivity analysis," *Remote Sensing of Environment*, vol. 22, pp. 209–233, 1987.
[12] J. W. Deardorff, "Efficient prediction of ground surface temperature and moisture with inclusion of a layer of vegetation," *J. Geophys. Res.*, vol. 83, no. 4, pp. 1889–1903, 1978.
[13] O. Taconet, T. Carlson, R. Bernard, and D. Vidal-Madjar, "Evaporation over an agricultural region using a surface flux/temperature model based on NOAA-AVHRR data," *J. Climate and Applied Meteorology*, vol. 25, pp. 284–307, 1986.
[14] J. Cesar, "Végétation, flore et valeur pastorale des savanes du parc national de la Comoé," Rapport du ministère de la recherche scientifique de Ivory Coast (Bouaké), 1978.
[15] D. S. Bartlett, G. J. Whiting, J. M. Hartman, "Use of vegetation indices to estimate intercepted solar radiation and net carbon dioxide exchange of a grass canopy," *Remote Sensing of Environment*, vol. 30, pp. 115–128, 1990.
[16] A. H. Strahler, , C. E. Woodcock, and J. A. Smith, "On the nature of models in remote sensing," *Remote Sensing of Environment*, vol. 20, pp. 121–139, 1986.
[17] A. Aman, F. Lavenu, A. Podaire, G. Saint *et al.*, "Etude de la production primaire des différentes savanes: apport des images haute résolution spatiale XS et TM," *Bull. de la Societé Francaise de Photogrammétrie*, pp. 40–44, 1989.
[18] F. Lavenu, "Télédétection et végetation tropicale. Exemple du Nord-Est de la Ivory Coast et des mangroves du Bangladesh," Ph.D. thesis, 1984.
[19] C. E. Woodcock, A. Strahler, and D. Jupp, "The factor of scale in remote sensing," *Remote Sensing of Environment*, vol. 21, pp. 311–332, 1987.
[20] X. N. Kong and D. Vidal-Madjar, "Effet de la résolution spatiale sur des propriétés statistiques des images satellites: une étude de cas," *Int. J. Remote Sensing*, vol. 8, pp. 1315–1328, 1988.
[21] B. N. Holben, "Characteristics of maximum-value composite images from temporal AVHRR data," *Int. J. Remote Sensing*, vol. 7, no. 11, pp. 1417–1434, 1986.
[22] A. R. Huete, R. D. Jackson, and D. F. Post, "Spectral response of a plant canopy with different backgrounds," *Remote Sensing of Environment*, vol. 17, pp. 37–53, 1985.

Angora Aman received the M.S. degree in physics from the University of Sciences of Abidjan, Ivory Coast, in 1985 and the Ph.D. degree from the University of Toulouse in 1991.

He is now Assistant Professor in the Physics Department of the University of Abidjan. His work has focused mainly on the problem of scaling in remote sensing.

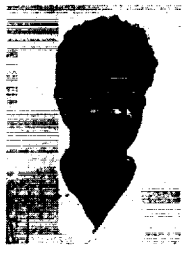

Heremino Paoly Randriamanantena received the B.S. degree in mathematics from the University of Antananarivo, Madagascar, in 1983 and the diploma of Engineer in Meteorology from the French School of Meteorology in 1986. He is presently preparing the Ph.D. degree at the Centre National de la Recherche en Météorologie and the Laboratoire d'Etudes et de Recherches en Télédétection Spatiale, Toulouse, working mainly on the use of remote sensing data for parameterizing land–atmosphere interactions.

Alain Podaire received the diploma of Engineer in Fluid Mechanics from ENSEEIH Toulouse, in 1977 and the diploma of Doctor Engineer in Fluid Thermodynamics from the Institut National Polythechnique of Toulouse in 1981.

He joined the Centre National dEtudes Spatiales (CNES) in 1981 to participate in the SPOT Preparatory Programme and the Laboratoire d'Etudes et de Recherches en Télédétection Spatiale in 1984, where he conducted research on vegetation monitoring from remotely sensed data. Since 1991 he has been at the Earth and Environment Sciences Division of CNES, working as Project Scientist for the POLarization and Directionality of the Earth Reflectance instrument and in charge of global environment databases prospective.

Robert Frouin received the B.S. degree in 1978, the M.S. degree in 1979, and the Ph.D. degree in 1981, all in physics and all from the University of Lille .

He joined the California Space Institute, Scripps Institution of Oceanography in 1983. As an assistant research meteorologist, he is conducting research in radiative transfer, primary productivity, land–atmosphere and ocean–atmosphere interactions, trace gas emissions to the atmospherè, and eastern boundary currents.